Instability in strongly magnetized accretion discs: A global perspective

Upasana Das, Mitchell C. Begelman, Geoffroy Lesur

Monthly Notices
of the
ROYAL ASTRONOMICAL SOCIETY

MNRAS **473,** 2791–2812 (2018)
Advance Access publication 2017 September 27

doi:10.1093/mnras/stx2518

Instability in strongly magnetized accretion discs: a global perspective

Upasana Das,[1]★ Mitchell C. Begelman[1,2] and Geoffroy Lesur[1,3,4]†

[1]*JILA, University of Colorado and National Institute of Standards and Technology, 440 UCB, Boulder, CO 80309-0440, USA*
[2]*Department of Astrophysical and Planetary Sciences, University of Colorado, 391 UCB, Boulder, CO 80309-0391, USA*
[3]*Université Grenoble Alpes, IPAG, F-38000 Grenoble, France*
[4]*CNRS, IPAG, F-38000 Grenoble, France*

Accepted 2017 September 25. Received 2017 September 5; in original form 2017 July 18

ABSTRACT

We examine the properties of strongly magnetized accretion discs in a global framework, with particular focus on the evolution of magnetohydrodynamic instabilities such as the magnetorotational instability (MRI). Work by Pessah & Psaltis showed that MRI is stabilized beyond a critical toroidal field in compressible, differentially rotating flows and, also, reported the appearance of two new instabilities beyond this field. Their results stemmed from considering geometric curvature effects due to the suprathermal background toroidal field, which had been previously ignored in weak-field studies. However, their calculations were performed under the local approximation, which poses the danger of introducing spurious behaviour due to the introduction of global geometric terms in an otherwise local framework. In order to avoid this, we perform a global eigenvalue analysis of the linearized MHD equations in cylindrical geometry. We confirm that MRI indeed tends to be highly suppressed when the background toroidal field attains the Pessah–Psaltis limit. We also observe the appearance of two new instabilities that emerge in the presence of highly suprathermal toroidal fields. These results were additionally verified using numerical simulations in PLUTO. There are, however, certain differences between the the local and global results, especially in the vertical wavenumber occupancies of the various instabilities, which we discuss in detail. We also study the global eigenfunctions of the most unstable modes in the suprathermal regime, which are inaccessible in the local analysis. Overall, our findings emphasize the necessity of a global treatment for accurately modelling strongly magnetized accretion discs.

Key words: accretion, accretion discs – instabilities – MHD.

1 INTRODUCTION

The magnetorotational instability (MRI; Balbus & Hawley 1991, 1998), which occurs in differentially rotating plasmas threaded by a weak magnetic field, is believed to explain the long-standing puzzle of the origin of turbulence and angular momentum transport in hydrodynamically stable accretion discs around compact objects. Most of the accretion disc studies so far have focused on the weak-field regime corresponding to plasma $\beta \gg 1$, where $\beta \equiv P/P_{\rm B}$, P and $P_{\rm B}$ being the gas and the (total) magnetic pressures, respectively. This is probably due to the apparent difficulty in explaining the generation and sustenance of a strong magnetic field therein. However, there is growing evidence, from both numerical simulations and observations, of accretion flows having suprathermal magnetic fields ($\beta < 1$).

For instance, Miller & Stone (2000) carried out three-dimensional vertically stratified shearing box simulations and studied the evolution of initially subthermal magnetic fields in the disc mid-plane having different geometries, namely, purely toroidal, zero net vertical flux and a uniform vertical field. They reported the formation of magnetically dominated ($\beta < 1$) coronae above 2 scaleheights from the disc mid-plane for the first two cases, due to the amplification of the magnetic field by MRI and its subsequent rise due to magnetic buoyancy. They also observed the formation of a large-scale field structure in both the disc and the corona, which was dominated by the toroidal field component. For the uniform vertical field case, they found both the corona and the disc to be magnetically dominated. However, this analysis was limited to the linear regime only, due to numerical difficulties arising from the generation of the disruptive MRI channel flow and, hence, is inconclusive. Bai & Stone (2013) carefully avoided the generation of the MRI channel flow in their vertically stratified shearing box simulations, which

★ E-mail: upasana.das@jila.colorado.edu
† JILA Visiting Fellow.

enabled them to reach very high initial net vertical fluxes. They found the entire disc to be magnetically dominated for initial vertical fields stronger than the threshold value of $\beta \sim 10^3$ at the mid-plane. More importantly, they observed the generation of a large-scale toroidal field that became suprathermal for such a strong initial vertical flux – the resulting time-averaged β being in the range 0.1–1 (see e.g. fig. 3 of Bai & Stone 2013) – a result that is of particular relevance to this work. More recently, Salvesen et al. (2016a,b) carried out comprehensive stratified shearing box simulations by extending the work of Bai & Stone (2013), in order to further explore the properties of MRI turbulence and dynamo activity in strongly magnetized accretion discs. Their results indicate the necessity of a net initial vertical flux in order to yield a magnetically dominated steady-state accretion disc, which is required by the dynamo to continuously regenerate and sustain the buoyantly escaping toroidal field (also verified by the global disc simulations of Fragile & Sądowski 2017). An important aspect of a strongly magnetized disc is the possibility of magnetocentrifugally driven outflows. Lesur, Ferreira & Ogilvie (2013) studied stratified shearing box simulations of an accretion disc having a strong poloidal field with $\beta \sim 10$, and found a comprehensible link between MRI and the generation of disc winds (also, see Moll 2012; Fromang et al. 2013; Bai & Stone 2013; Riols et al. 2016). There have also been observations of strongly magnetized winds in black hole binaries such as GRO J1655−40 (Miller et al. 2006) and GRS 1915+105 (Miller et al. 2016), indicative of the probable existence of an underlying strongly magnetized disc from which the winds are launched.

Strongly magnetized accretion discs have been theoretically shown to be viscously and thermally stable (Begelman & Pringle 2007; Oda et al. 2009; Sądowski 2016), a result which might finally lead to a fruitful resolution of the mismatch between observations and theoretical predictions of the standard α-disc model (Shakura & Sunyaev 1973, 1976; Lightman & Eardley 1974). Magnetically dominated discs are also less dense than their weakly magnetized counterparts, which makes them more stable against fragmentation under self-gravity (Pariev, Blackman & Boldyrev 2003). This in turn can prevent the clumping of the infalling gas and aid the fuelling of active galactic nuclei and the growth of supermassive black hole seeds (Begelman & Pringle 2007; Gaburov, Johansen & Levin 2012). Strongly magnetized discs can also explain the larger than expected vertical scaleheights, inflow speeds and colour temperatures inferred for accretion discs in systems such as cataclysmic variables and some X-ray binaries (Begelman & Pringle 2007), as well as several key aspects of X-ray binary state transitions, which are otherwise unresolved in the standard disc theory (Begelman, Armitage & Reynolds 2015).

Given the likely importance of strong magnetic fields in accretion discs, it is essential to determine whether and how the instabilities like MRI are affected in this regime. Pessah & Psaltis (2005, hereafter PP05) showed by means of a local linear stability analysis that suprathermal toroidal magnetic fields (in the presence of a highly subthermal poloidal field) have a profound effect on the stability of large vertical wavenumber, axisymmetric perturbations, which correspond to the most unstable modes of conventional MRI. They demonstrated that this was mainly due to the important roles played by both the curvature of the toroidal field lines and compressibility when $\beta < 1$ – either or both effects being largely ignored in weak-field studies (see e.g. Balbus & Hawley 1991, 1992, 1998; Blaes & Balbus 1994; Balbus 1995, and PP05 for a detailed comparison). Interestingly, their study identified a critical toroidal Alfvén speed for purely Keplerian flows, beyond which MRI starts to get stabilized at small vertical wavenumbers (i.e. $v_{\mathrm{A}\phi}^{\mathrm{PP1}} = \sqrt{v_{\mathrm{K}} c_{\mathrm{s}}}$, where $v_{\mathrm{A}\phi}^{\mathrm{PP1}}$, v_{K} and c_{s} are the critical toroidal Alfvén velocity, Keplerian velocity and sound speed, respectively) and is eventually completely suppressed, across the entire range of allowed vertical wavenumbers, at a slightly higher critical value (i.e. $v_{\mathrm{A}\phi}^{\mathrm{PP2}} = \sqrt{2 v_{\mathrm{K}} c_{\mathrm{s}}}$). Additionally, they reported the emergence of two new suprathermal instabilities, beyond $v_{\mathrm{A}\phi}^{\mathrm{PP2}}$, that occupy different wavenumber regimes. Such an upper limit on the magnetic field strength for MRI to operate is quite appealing as, if correct, it not only helps constrain the theory better, but also provides testable predictions. However, since PP05 carried out their analysis under the local approximation, one cannot be confident regarding the robustness of their findings. This is because incorporating global curvature terms in a local framework often leads to spurious outcomes.

Our main aim in this work is to revisit the analysis by PP05 and reassess their main results in a global framework, which is a necessary step before extending the model to add more complex physics. In order to do so, we solve the global, linear eigenvalue problem for a compressible, axisymmetric, magnetized fluid in cylindrical disc geometry. This also allows us to systematically compare the results in the two formalisms (also, see Curry, Pudritz & Sutherland 1994; Latter, Fromang & Faure 2015, for the connection between local and global weak-field MRI modes). In our analysis, we find that MRI indeed tends to be highly suppressed for sufficiently suprathermal toroidal background fields. However, unlike PP05, we observe only a partial reduction in the MRI growth rate at small vertical wavenumbers when the background toroidal Alfvén velocity exceeds $v_{\mathrm{A}\phi}^{\mathrm{PP1}}$. In fact, as long as MRI operates in the global analysis, it spans the entire range of allowed vertical wavenumbers. We also observe the appearance of two new instabilities, as predicted by PP05, when the background toroidal Alfvén velocity exceeds $v_{\mathrm{A}\phi}^{\mathrm{PP2}}$. However, the global results exhibit a very different variation of growth rate as a function of vertical wavenumber for these two instabilities. Overall, it appears that the local analysis predicts the maximum possible growth rates of the various instabilities in the suprathermal regime reasonably well, but falls short in estimating the range of vertical wavenumbers occupied by them. Nevertheless, this is an important confirmation, since a local analysis, if valid to a reasonable degree, gives us a much better understanding of the underlying stability criteria. We further carry out a small set of simulations using the finite-volume code PLUTO (Mignone et al. 2007), which corroborates the results from our global eigenvalue analysis. The current work is the first in a series of explorations, which include additional effects such as non-axisymmetry, and radial and vertical stratification in a strongly magnetized disc.

In this context, we mention that Curry & Pudritz (1995) carried out one of the earlier global, linear stability analyses of a differentially rotating flow to study the effect of a strong toroidal magnetic field. They also noted the progressive stabilization of MRI with increasing toroidal field strength. However, their work considered only *incompressible* flows (additionally having radial stratification) and, hence, some of their conclusions differ from those of PP05. For instance, the critical toroidal Alfvén speed for complete MRI stabilization according to Curry & Pudritz (1995) is given by the rotational speed of the flow, which is justified as it is the only velocity scale in the absence of compressibility. They also reported the appearance of a new instability called the large field instability (LFI), which we will discuss later in

Section 5.2.1. Thus, compressibility along with magnetic curvature seems to play an important role in determining the stability of a strongly magnetized accretion flow.

We also mention here the linear stability analysis of an axisymmetric accretion flow carried out by Terquem & Papaloizou (1996, hereafter TP96) in the presence of a purely toroidal, but subthermal magnetic field, and vertical and radial stratification. They performed local as well as global analyses and found the results of the two cases to be in good agreement with each other. They observed mainly two kinds of instabilities for the extreme limits of their local dispersion relation. When the ratio of radial to vertical wavenumber was large, a Parker-type instability was observed, driven by vertical magnetic buoyancy. On the other hand, when the ratio of radial to vertical wavenumber was small, a shear-driven instability prevailed, even in the absence of stratification. They also noted that both kinds of instabilities were highly localized in the radial coordinate. The local dispersion relation derived in this work generalizes the one derived by TP96 by including a uniform background poloidal field, although it does not include vertical stratification (see Appendix B). However, suprathermal background toroidal fields, together with a subthermal poloidal field and no vertical stratification, yield very different instabilities in our work. We still obtain shear-driven modes but do not observe magnetic vertical buoyancy-driven modes (due to the absence of vertical stratification in our work). We instead observe the appearance of radial buoyancy-driven modes, due to the radial tension force from the suprathermal toroidal field (also, see Kim & Ostriker 2000, in a subthermal context), which we elaborate below.

This paper is organized as follows. In Section 2, we lay out the linearized MHD equations that form the basis of our analysis. In Section 3, we focus on developing a self-consistent local theory and present the calculations leading to a generic local dispersion relation, which includes the effects of magnetic curvature, compressibility, non-axisymmetry and background radial gradients. We also obtain the PP05 limit of our local dispersion relation in order to compare with the global analysis. In Section 4, we describe in detail the numerical set-up and normalization scheme used for our global eigenvalue analysis. In Section 5, we present the solutions of the global eigenvalue problem. We first recall the stability criteria from local theory and, then, systematically analyse the global properties, including the global eigenfunctions, of the *most* unstable modes of the instabilities in the suprathermal regime. In Section 6, we present the results of a small set of numerical simulations performed using PLUTO and compare them with our global eigenvalue analysis. We conclude in Section 7, by highlighting our main results and discussing some of their implications, which readers may refer to at any point for a brief summary of this work.

2 LINEARIZED MHD EQUATIONS OF MOTION

We begin by recalling the ideal MHD equations characterizing a magnetized, compressible accretion flow

$$\frac{\partial \rho}{\partial t} + \nabla \cdot (\rho \boldsymbol{v}) = 0, \tag{1}$$

$$\frac{\partial \boldsymbol{v}}{\partial t} + (\boldsymbol{v} \cdot \nabla)\boldsymbol{v} + \nabla\Phi + \frac{1}{\rho}\nabla\left(P + \frac{\boldsymbol{B}^2}{8\pi}\right) - \frac{1}{4\pi\rho}(\boldsymbol{B} \cdot \nabla)\boldsymbol{B} = 0, \tag{2}$$

$$\frac{\partial \boldsymbol{B}}{\partial t} - \nabla \times (\boldsymbol{v} \times \boldsymbol{B}) = 0, \tag{3}$$

where ρ is the density, P the gas pressure, Φ the gravitational potential of the central object, $\boldsymbol{B}$ the magnetic field and $\boldsymbol{v}$ the fluid velocity. We adopt a cylindrical coordinate system (r, ϕ, z) and an axisymmetric background having $\boldsymbol{v} = (0, v_{0\phi}(r), 0)$ and $\boldsymbol{B} = (0, B_{0\phi}(r), B_{0z})$, where B_{0z} is a constant and the other flow variables are assumed to depend on r only. We neglect vertical stratification and vertical gravity, and assume the gravitational potential to be cylindrical such that $\Phi = -GM/r$. The above equations are also supplemented by an equation of state, $P = P(\rho)$. We furthermore neglect self-gravity of the disc, as well as any dissipative processes.

In order to carry out a linear stability analysis, we perturb equations (1)–(3) in Eulerian coordinates and retain only the perturbed amplitudes of linear order such that

$$\rho = \rho_0 + \rho_1, \tag{4}$$

$$P = P_0 + P_1, \tag{5}$$

$$\boldsymbol{v} = \boldsymbol{v}_0 + \boldsymbol{v}_1, \tag{6}$$

$$\boldsymbol{B} = \boldsymbol{B}_0 + \boldsymbol{B}_1. \tag{7}$$

Note that whereas the vertical equilibrium is trivial in the absence of any vertical stratification, the radial equilibrium is derived from equation (2) as

$$\Omega^2 = \Omega_{\rm K}^2 + \frac{v_{{\rm A}\phi}^2}{r^2}\left(1 + \frac{\partial \ln B_{0\phi}}{\partial \ln r}\right) + \frac{1}{r\rho_0}\partial_{\rm r} P_0, \tag{8}$$

where, $\Omega = v_{0\phi}/r$ is the background angular velocity, $\Omega_{\rm K} = \sqrt{(GM/r^3)}$ the Keplerian rotation frequency and $v_{{\rm A}\phi} = B_{0\phi}/\sqrt{(4\pi\rho_0)}$ the toroidal Alfvén velocity. Thus, we see that such a disc may deviate significantly from purely Keplerian rotation, especially if it is strongly magnetized. However, Keplerian rotation is recovered in the absence of background radial gradients and for $v_{{\rm A}\phi} \ll v_{\rm K}$, where $v_{\rm K} = \sqrt{(GM/r)}$ is the Keplerian velocity.

We now write below the complete set of the linearized MHD equations:

$$\partial_{\rm t}\rho_1 + \rho_0\left[\frac{1}{r}\partial_{\rm r}(r v_{1{\rm r}}) + \frac{1}{r}\partial_\phi v_{1\phi} + \partial_{\rm z} v_{1{\rm z}}\right] + \Omega\partial_\phi\rho_1 + v_{1{\rm r}}\partial_{\rm r}\rho_0 = 0, \tag{9}$$

$$\rho_0[\partial_{\rm t} v_{1{\rm r}} + \Omega\partial_\phi v_{1{\rm r}} - 2\Omega v_{1\phi}] + \partial_{\rm r} P_1 + \frac{1}{4\pi}\left[B_{0\phi}\partial_{\rm r}B_{1\phi} + B_{1\phi}\partial_{\rm r}B_{0\phi} - \frac{B_{0\phi}}{r}\partial_\phi B_{1{\rm r}} - B_{0{\rm z}}\partial_{\rm z}B_{1{\rm r}} + B_{0{\rm z}}\partial_{\rm r}B_{1{\rm z}} + \frac{2B_{0\phi}B_{1\phi}}{r}\right]$$
$$- \frac{\rho_1}{\rho_0}\left[\frac{B_{0\phi}^2}{4\pi r} + \partial_{\rm r}P_0 + \frac{B_{0\phi}}{4\pi}\partial_{\rm r}B_{0\phi}\right] = 0, \tag{10}$$

$$\rho_0[\partial_{\rm t} v_{1\phi} + v_{1{\rm r}}(r\partial_{\rm r}\Omega) + 2\Omega v_{1{\rm r}} + \Omega\partial_\phi v_{1\phi}] + \frac{1}{r}\partial_\phi P_1 - \frac{1}{4\pi}\left[B_{1{\rm r}}\partial_{\rm r}B_{0\phi} + B_{0{\rm z}}\partial_{\rm z}B_{1\phi} - \frac{B_{0{\rm z}}}{r}\partial_\phi B_{1{\rm z}} + \frac{B_{0\phi}B_{1{\rm r}}}{r}\right] = 0, \tag{11}$$

$$\rho_0[\partial_{\rm t} v_{1{\rm z}} + \Omega\partial_\phi v_{1{\rm z}}] + \partial_{\rm z} P_1 + \frac{1}{4\pi}\left[B_{0\phi}\partial_{\rm z}B_{1\phi} - \frac{B_{0\phi}}{r}\partial_\phi B_{1{\rm z}}\right] = 0, \tag{12}$$

$$\partial_{\rm t}B_{1{\rm r}} + \Omega\partial_\phi B_{1{\rm r}} - \frac{B_{0\phi}}{r}\partial_\phi v_{1{\rm r}} - B_{0{\rm z}}\partial_{\rm z}v_{1{\rm r}} = 0, \tag{13}$$

$$\partial_{\rm t}B_{1\phi} + v_{1{\rm r}}\partial_{\rm r}B_{0\phi} + \Omega\partial_\phi B_{1\phi} - B_{1{\rm r}}(r\partial_{\rm r}\Omega) - B_{0{\rm z}}\partial_{\rm z}v_{1\phi} + B_{0\phi}\partial_{\rm z}v_{1{\rm z}} + B_{0\phi}\partial_{\rm r}v_{1{\rm r}} = 0, \tag{14}$$

$$\partial_{\rm t}B_{1{\rm z}} + \Omega\partial_\phi B_{1{\rm z}} - \frac{B_{0\phi}}{r}\partial_\phi v_{1{\rm z}} + \frac{B_{0{\rm z}}}{r}\partial_\phi v_{1\phi} + \frac{B_{0{\rm z}}}{r}\partial_{\rm r}(r v_{1{\rm r}}) = 0. \tag{15}$$

Note that the above set of equations is quite generic, encompassing non-axisymmetric perturbations, background radial gradients, compressibility and magnetic curvature effects, and is generally applicable for any magnetic field strength. We can now use the same linearized system of equations to derive a local dispersion relation, as well as solve the global eigenvalue problem.

3 LOCAL ANALYSIS

In this section, we present a systematic derivation of the local dispersion relation from the set of equations (9)–(15), which differs from the approach employed by PP05. We apply a more physically motivated WKB formalism and, also, account for the radial dependence of the normal modes in the system to the requisite order (as both the amplitude and radial wavenumber of the modes should in general be functions of radius when there is a radially varying background). We explicitly include the magnetic tension in the background flow such that it is no longer purely Keplerian in the strongly magnetized limit, in order to make the global analysis self-consistent. Additionally, we obtain a more generic dispersion relation containing the effects of non-axisymmetry and background radial gradients. We discuss some of the well-known limiting cases of our local dispersion relation in Appendix B.

3.1 Analytical approximation scheme

Before proceeding further, we first apply certain physically motivated assumptions that simplify the problem and make the solutions analytically tractable. We also define some new variables for a more compact visualization during the analysis in the present section, which are listed in Table 1.

(i) We assume that the perturbations are adiabatic such that the energy equation is given by

$$\dot{P}_1 - c_{\rm s}^2\dot{\rho}_1 = -(\gamma P_0)(\boldsymbol{v}_1\cdot\boldsymbol{S}), \tag{16}$$

where the overdot represents time derivative, $c_{\rm s} = \sqrt{\gamma P/\rho}$ is the local sound speed, γ the adiabatic index and $\boldsymbol{S}$ the Schwarzschild discriminant vector or non-adiabacity of the fluid given by

$$\boldsymbol{S} = \nabla\left(\ln\frac{P_0^{1/\gamma}}{\rho_0}\right). \tag{17}$$

Table 1. Summary of the dimensionless parameters introduced (and to be used only) in Section 3, and Appendices A and B of this work.

$\eta = k_z r \frac{B_{0z}}{B_{0\phi}}$		$\boldsymbol{b} = \frac{\boldsymbol{B}_1}{B_{0\phi}}$	
$\hat{B}_\phi = \frac{\partial \ln B_{0\phi}}{\partial \ln r}$		$q = -\frac{\partial \ln \Omega}{\partial \ln r}$	Shear parameter
$\beta = \frac{8\pi P_0}{B_{0\phi}^2}$	Plasma-beta	$n = m + \eta$	
$\boldsymbol{u} = \left(\frac{\rho_0}{\gamma P_0}\right)^{1/2} \boldsymbol{v}_1 \equiv \frac{1}{c_s}\boldsymbol{v}_1$		$x = \frac{\gamma\beta}{2}$	
$\{\tilde{\omega}, \tilde{\Omega}, \tilde{\kappa}, \tilde{\Omega}_K\} = \frac{r}{c_s}\{\omega, \Omega, \kappa, \Omega_K\}$		$\tilde{\kappa}^2 = 2\tilde{\Omega}^2(2-q)$	Epicyclic frequency
$\mu = \tilde{\omega} - m\tilde{\Omega}$		$y = \tilde{\Omega}^2 - \tilde{\Omega}_K^2$	

For simplicity, we will assume that the background is adiabatic so that $\boldsymbol{S} = 0$ (see Appendix A for a more general case) and we simply have

$$P_1 = \frac{\gamma P_0}{\rho_0}\rho_1 = c_s^2 \rho_1. \tag{18}$$

(ii) We assume the perturbed variables to have the form

$$f_i = f_i(r) \exp i(m\phi + k_z z - \omega t) \tag{19}$$

such that invoking the WKB approximation we can write

$$\partial_r f_i = i l f_i + g_i(r), \quad g_i = \mathcal{O}\left(\frac{1}{r}\right), \tag{20}$$

where ω is the modal frequency, t the time, l, m and k_z the radial, azimuthal and vertical wavenumbers (all constants) respectively. We focus on large wavenumber modes such that $lr, k_z r \gg 1$ and, also, $g_i(r)$ is assumed to be small in the WKB sense such that $|g_i(r)| \ll l f_i$. We note here that while considering radial derivatives of the perturbations, PP05 considered only the ilf_i terms in equation (20) and, as a result, our conclusions differ from theirs in the large l/k_z limit, as discussed below.

(iii) We furthermore follow the orderings stated in Begelman (1998) such that

$$k_z^2 r^2 \gg 1 + m^2, \quad k_z = \mathcal{O}(l), \tag{21}$$

$$|\omega^2| \ll k_z^2 c_s^2, \quad k_z v_{1z} + l v_{1r} = \mathcal{O}\left(\frac{v_{1r}}{r}\right), \tag{22}$$

$$B_{0z} \ll B_{0\phi}, \quad B_{0z} l,\, B_{0z} k_z = \mathcal{O}\left(\frac{B_{0\phi}}{r}\right), \tag{23}$$

which further allows us to write

$$v_{1z} \approx -\frac{l}{k_z} v_{1r} \quad \text{and} \quad B_{1z} \approx -\frac{l}{k_z} B_{1r}. \tag{24}$$

(iv) Note that the equations (9)–(15) would yield a dispersion relation that is a sixth-degree polynomial in ω, whose six solutions correspond to two fast magnetosonic modes, two Alfvén modes and two slow magnetosonic modes. However, the fast magnetosonic modes lie well separated from the Alfvén and slow magnetosonic modes in the ω–k_z space (as we shall indeed see later) and, hence, can be neglected in our analysis with the aim of simplifying the derivation and obtaining some useful analytical insights. We do so by assuming condition (22), which can be interpreted as neglecting the acceleration term in the vertical force balance equation. This eventually yields a reduced fourth-degree dispersion relation in ω.

3.2 Local dispersion relation

We are now in a position to work towards obtaining a dispersion relation. Note that f_i and g_i from equations (19) and (20) are presumably different for the different perturbed quantities. However, in the following analysis, we try to handle this issue by eliminating entire radial derivative terms to the required order, by combining the right equations wherever possible. First, following Begelman (1998), we combine the r- and z-components of the momentum balance equations (10) and (12). Under the approximation scheme detailed in the previous section, and using equations (8), (18) and the notation from Table 1, these two equations can be written as respectively

$$\rho_0[i(m\Omega - \omega)v_{1r} - 2\Omega v_{1\phi}] = -\partial_r P_1 + P_1 \frac{\rho_0}{\gamma P_0} r(\Omega^2 - \Omega_K^2) + \frac{B_{0\phi}}{4\pi r}\left\{ i\left[m + \eta\left(1 + \frac{l^2}{k_z^2}\right)\right] B_{1r} - (2 + \hat{B}_\phi) B_{1\phi} - r\partial_r B_{1\phi} \right\} \tag{25}$$

and

$$i\rho_0(m\Omega-\omega)v_{1z}=-ik_z\left(P_1+\frac{B_{0\phi}B_{1\phi}}{4\pi}\right)+im\frac{B_{0\phi}B_{1z}}{4\pi r}. \tag{26}$$

Next, we multiply equation (25) by $-ik_z$ and differentiate equation (26) with respect to r, and add the results. The terms involving $\partial_r(P_1+B_{0\phi}B_{1\phi}/4\pi)$ cancel, and then by invoking equations (20) and (24), we obtain to the requisite order

$$\rho_0\left[(m\Omega-\omega)\left(1+\frac{l^2}{k_z^2}\right)v_{1r}+2i\Omega v_{1\phi}\right]=\frac{B_{0\phi}}{4\pi r}\left[2iB_{1\phi}+(m+\eta)\left(1+\frac{l^2}{k_z^2}\right)B_{1r}\right]-iP_1\frac{\rho_0}{\gamma P_0}r(\Omega^2-\Omega_K^2). \tag{27}$$

Note that, with appropriate modifications, e.g. converting $\boldsymbol{B}_1$ to $\dot{\boldsymbol{B}}_1$, equation (27) reduces to equation (3.25) of Begelman (1998) in the absence of rotation and gravity.

For the remainder of the analysis, we can neglect the terms involving v_{1z} and B_{1z} in equation (26) (see Section 3.1) such that P_1 can be eliminated as

$$P_1=-\frac{B_{0\phi}B_{1\phi}}{4\pi}. \tag{28}$$

We can also use the r-component of the induction equation given by equation (13), to eliminate B_{1r} in favour of v_{1r} as

$$(m\Omega-\omega)B_{1r}=\frac{B_{0\phi}}{r}(m+\eta)v_{1r}. \tag{29}$$

We then apply equations (28) and (29) to equation (27). We further define dimensionless parameters β, $\tilde{\omega}$, $\tilde{\Omega}$, μ and $\boldsymbol{b}$ as given in Table 1, in order to non-dimensionalize all ensuing equations in this section. Thus, equation (27) reduces to

$$\left[\frac{\gamma\beta}{2}\mu^2-(m+\eta)^2\right]\left(1+\frac{l^2}{k_z^2}\right)\frac{u_r}{2}-i\mu\frac{\gamma\beta}{2}\tilde{\Omega}u_\phi=-i\left[1+\frac{1}{2}(\tilde{\Omega}^2-\tilde{\Omega}_K^2)\right]\mu b_\phi. \tag{30}$$

We can now eliminate b_ϕ in favour of $\nabla\cdot\boldsymbol{u}$ through the continuity equation as follows. First, we non-dimensionalize equation (9) in terms of the new variables given in Table 1 and use equation (18) to write ρ_1 in terms of P_1. Next, we rewrite the radial equilibrium condition given by equation (8) in terms of the new variables, and using it together with equation (28) to replace P_1 in the continuity equation we obtain

$$-i\mu b_\phi=\frac{\gamma\beta}{2}r(\nabla\cdot\boldsymbol{u})-(1+\hat{B}_\phi)u_r+\frac{\gamma\beta}{2}(\tilde{\Omega}^2-\tilde{\Omega}_K^2)u_r. \tag{31}$$

Hence, equation (30) then becomes

$$\left[\frac{\gamma\beta}{2}\mu^2-(m+\eta)^2\right]\left(1+\frac{l^2}{k_z^2}\right)\frac{u_r}{2}-i\mu\frac{\gamma\beta}{2}\tilde{\Omega}u_\phi=\left[1+\frac{1}{2}(\tilde{\Omega}^2-\tilde{\Omega}_K^2)\right]\left[\frac{\gamma\beta}{2}r(\nabla\cdot\boldsymbol{u})-(1+\hat{B}_\phi)u_r+\frac{\gamma\beta}{2}(\tilde{\Omega}^2-\tilde{\Omega}_K^2)u_r\right], \tag{32}$$

which reduces to equations (3.26) and (3.29) of Begelman (1998) in the non-rotating and no-gravity limits.

The ϕ-component of the induction equation given by equation (14) can be simplified (to requisite order) by using equations (29) and (31) as

$$i(m+\eta)u_\phi=\left(1+\frac{\gamma\beta}{2}\right)r(\nabla\cdot\boldsymbol{u})-\left[2-\left(\frac{m+\eta}{\mu}\right)\tilde{\Omega}\frac{\partial\ln\Omega}{\partial\ln r}-\frac{\gamma\beta}{2}(\tilde{\Omega}^2-\tilde{\Omega}_K^2)\right]u_r. \tag{33}$$

The above equation reduces to equation (3.28) of Begelman (1998) in the non-rotating and no-gravity limits.

Under our approximation scheme, the ϕ-component of the momentum balance equation given by equation (11) can be written after using equations (29) and (31) as

$$i\mu^2u_\phi=(m+\eta)r(\nabla\cdot\boldsymbol{u})+\left[\frac{\tilde{\kappa}^2}{2\tilde{\Omega}}\mu+(m+\eta)(\tilde{\Omega}^2-\tilde{\Omega}_K^2)\right]u_r, \tag{34}$$

where $\kappa^2=2\Omega^2(2+\partial\ln\Omega/\partial\ln r)$ is the epicyclic frequency and $\tilde{\kappa}$ the corresponding dimensionless parameter defined in Table 1. Equation (34) reduces to equation (3.30) of Begelman (1998) in the non-rotating and no-gravity limits.

Equations (32)–(34) form a system of three homogeneous linear equations in the variables $\{u_r, r(\nabla\cdot\boldsymbol{u}), iu_\phi\}$. To further simplify the notation, we introduce the parameters q, n, x and y, which are also defined in Table 1. Equations (32)–(34) then become:

$$\left[\frac{1}{2}(x\mu^2-n^2)\left(1+\frac{l^2}{k_z^2}\right)+\left(1+\frac{y}{2}\right)(1+\hat{B}_\phi-xy)\right]u_r-x\left(1+\frac{y}{2}\right)r(\nabla\cdot\boldsymbol{u})-x\mu\tilde{\Omega}(iu_\phi)=0, \tag{35}$$

$$\left(2+q\frac{n}{\mu}\tilde{\Omega}-xy\right)u_r-(1+x)r(\nabla\cdot\boldsymbol{u})+n(iu_\phi)=0 \tag{36}$$

and

$$[(2-q)\tilde{\Omega}\mu+ny]u_r+nr(\nabla\cdot\boldsymbol{u})-\mu^2(iu_\phi)=0. \tag{37}$$

We can eliminate $r(\nabla\cdot\boldsymbol{u})$ in equation (35) by using equation (37) to obtain

$$\left[\frac{1}{2}(x\mu^2-n^2)\left(1+\frac{l^2}{k_z^2}\right)+\left(1+\frac{y}{2}\right)\left(1+\hat{B}_\phi+\frac{2-q}{n}x\tilde{\Omega}\mu\right)\right]u_{\rm r}-\left[\tilde{\Omega}+\frac{\mu}{n}\left(1+\frac{y}{2}\right)\right]x\mu(iu_\phi)=0. \tag{38}$$

We next express u_ϕ in terms of $u_{\rm r}$ by eliminating $r(\nabla\cdot\boldsymbol{u})$ between equations (36) and (37). This is achieved by multiplying equation (36) by n and equation (37) by $(1+x)$ and adding the results to yield

$$-iu_\phi=\left[\frac{2n\left(1+\frac{y}{2}\right)+(1+x)(2-q)\tilde{\Omega}\mu+\frac{n^2}{\mu}q\tilde{\Omega}}{n^2-(1+x)\mu^2}\right]u_{\rm r}. \tag{39}$$

Finally, we substitute equation (39) into equation (38), cancel the common factor of $u_{\rm r}$ and after some rearrangement obtain the (dimensionless) dispersion relation for the case including the effects of rotation, gravity, compressibility, background toroidal and poloidal fields, magnetic curvature and background radial gradients in an adiabatic background:

$$\left[(x\mu^2-n^2)\left(1+\frac{l^2}{k_z^2}\right)+(2+y)(1+\hat{B}_\phi)\right][n^2-(1+x)\mu^2]+2(2-q)x(1+x)\mu^2\tilde{\Omega}^2$$
$$+4\mu xn\tilde{\Omega}(2+y)+2n^2qx\tilde{\Omega}^2+x\mu^2(2+y)^2=0. \tag{40}$$

3.3 PP05 limit of the local dispersion relation

In order to compare with PP05, we need to obtain the axisymmetric strong $B_{0\phi}$ limit of our dispersion relation. Hence, we put $m=0$, $n=\eta$ and $\mu=\tilde{\omega}$ in the dispersion relation given by equation (40), which we further expand and divide throughout by $x(1+x)$.

We also use $\tilde{\kappa}^2=4\tilde{\Omega}^2-2q\tilde{\Omega}^2$ and assume $x\ll 1$. On further assuming $r\partial_{\rm r}P_0/(\gamma P_0)=\mathcal{O}(1)$ and $(1+\hat{B}_\phi)=\mathcal{O}(1)$, we obtain from equation (8)

$$y=\tilde{\Omega}^2-\tilde{\Omega}_{\rm K}^2\approx\frac{(1+\hat{B}_\phi)}{x}\gg 1. \tag{41}$$

On applying all the above orderings to equation (40), dimensionalizing it using the definitions in Table 1 and multiplying throughout by $c_{\rm s}^4/r^4$, we obtain

$$\left(1+\frac{l^2}{k_z^2}\right)\omega^4-\left[k_z^2v_{\rm Az}^2\left(1+\frac{l^2}{k_z^2}\right)+\kappa^2+(1-\hat{B}_\phi^2)\frac{v_{{\rm A}\phi}^2}{r^2}\right]\omega^2-4\Omega(k_zv_{\rm Az})(1+\hat{B}_\phi)\frac{v_{{\rm A}\phi}}{r}\omega$$
$$+k_z^2v_{\rm Az}^2\left[\frac{c_{\rm s}^2}{v_{{\rm A}\phi}^2}\left\{k_z^2v_{\rm Az}^2\left(1+\frac{l^2}{k_z^2}\right)+2\Omega^2\frac{\partial\ln\Omega}{\partial\ln r}\right\}-(1+\hat{B}_\phi)^2\frac{v_{A\phi}^2}{r^2}\right]=0. \tag{42}$$

Before we compare the above dispersion relation with that obtained by PP05, we point out that we non-dimensionalize our equations differently than PP05. PP05 assumed their background equilibrium flow to be purely Keplerian, instead of considering equation (8), which in the absence of radial gradients becomes

$$\Omega^2=\Omega_{\rm K}^2+\frac{v_{{\rm A}\phi}^2}{r^2}, \tag{43}$$

i.e. PP05 ignored the magnetic tension term in the background equilibrium flow, which becomes important when the toroidal field is strong. However, note that they did include the effect of curvature due to magnetic tension in their linear stability analysis (as do we). We, on the other hand, self-consistently non-dimensionalize all the frequencies with respect to the local $\Omega_{\rm K}$, all length-scales by the local radial coordinate r_0, all wavenumbers by $1/r_0$ and all velocities by $r_0\Omega_{\rm K}$. Then, the dimensionless equilibrium condition (43) becomes $\Omega^2=1+v_{{\rm A}\phi}^2$ (instead of $\Omega^2=1$, as in PP05), the term $2\Omega^2\partial\ln\Omega/\partial\ln r$ becomes $-3-2v_{{\rm A}\phi}^2$ (instead of $2\Omega^2\partial\ln\Omega/\partial\ln r=-3$, as in PP05) and the dimensionless epicyclic frequency becomes $\kappa^2=1+2v_{{\rm A}\phi}^2$ (instead of $\kappa^2=1$, as in PP05). Thus, using these, the dimensionless version of equation (42), in the limit $\hat{B}_\phi=0$, becomes

$$\left(1+\frac{l^2}{k_z^2}\right)\omega^4-\left[1+k_z^2v_{\rm Az}^2\left(1+\frac{l^2}{k_z^2}\right)+3v_{{\rm A}\phi}^2\right]\omega^2-4(k_zv_{\rm Az})(1+v_{{\rm A}\phi}^2)^{1/2}v_{{\rm A}\phi}\omega$$
$$+k_z^2v_{\rm Az}^2\left[\frac{c_{\rm s}^2}{v_{{\rm A}\phi}^2}\left\{k_z^2v_{\rm Az}^2\left(1+\frac{l^2}{k_z^2}\right)-3-2v_{{\rm A}\phi}^2\right\}-v_{{\rm A}\phi}^2\right]=0. \tag{44}$$

As a result of this difference in normalization, PP05 obtained higher growth rates for the unstable modes at stronger field strengths (see Fig. 2 below and compare the growth rates with those in fig. 2 of PP05).

First, let us compare the above dispersion relation with that given by equation (25) of PP05 in the limit $l^2/k_z^2\to 0$ (note that this limit does not violate the WKB approximation in our case as it only implies the special case $l^2\ll k_z^2$ but $l^2r^2\gg 1$ still holds true). On dividing equation (25) of PP05 throughout by $k_z^2v_{{\rm A}\phi}^2$, neglecting the fast modes by dropping the ω^6 term and by considering the strong field limit of

$v_{A\phi}^2 \gg \{c_s^2, v_{Az}^2\}$, one arrives at a fourth-degree dispersion relation in ω. This is given by equation (41) of PP05, which is equivalent to our equation (44) above, when the former is dimensionalized according to our aforementioned scheme and the curvature terms therein set to $\epsilon_i = 1$, with $i = 1, 2, 3$ and 4.

Next, we compare our dispersion relation given by equation (44) above with equation (25) of PP05 in the limit l/k_z is finite. We note that equation (25) of PP05 has some imaginary terms proportional to il/k_z^2. These terms, however, do not appear in our equation (44), which was derived self-consistently by retaining only the leading order WKB terms. In this context, we refer to Appendix A and fig. 12 of PP05, where they discussed the effect of a finite and constant l/k_z on their solutions. As the value of l/k_z increased, PP05 found a new instability having a constant growth rate independent of k_z, which they attributed to the terms proportional to il/k_z^2 in their dispersion relation. Note that we do not observe any such instability when solving with a finite l/k_z in our dispersion relation given by equation (44), nor do they appear in the global eigenvalue solutions (see Fig. 2 below).

4 GLOBAL EIGENVALUE ANALYSIS

4.1 Details of the numerical set-up

Note that since the primary aim of this work is to compare with the local analysis in the PP05 limit, we restrict ourselves to axisymmetric perturbations (i.e. $\partial_\phi = 0$ or $m = 0$) and ignore any radial stratification ($\partial_r \rho_0 = \partial_r B_{0\phi} = \hat{B}_\phi = 0$). However, both of these effects can be included in a numerical set-up similar to that described below, which will be the focus of our next work in this series.

For axisymmetric perturbations, the condition $\nabla \cdot \boldsymbol{B}_1 = 0$ is easily imposed by invoking the vector potential $\boldsymbol{A}$ with components (A_r, A_ϕ, A_z), and perturbing it such that $\boldsymbol{A} = \boldsymbol{A}_0 + \boldsymbol{A}_1$. This leads to $B_{1r} = -\partial_z A_{1\phi}$ and $B_{1z} = (1/r)\partial_r(r A_{1\phi})$, where $A_{1\phi}$ is the azimuthal component of the perturbed vector potential. This simplifies the system of equations (9)–(15) by eliminating one variable and, hence, the need for equation (15).

Now, in order to construct the global solutions from the linearized axisymmetric system of equations (9)–(14), we consider an annular section of the accretion disc, which exhibits differential rotation and is bounded in radius $r \in [R_{in}, R_{out}]$, such that all the radial curvature terms can be included. This region is assumed to be located far from the influence of the central object as well as from the exteriors of the disc. The solutions are decomposed on a basis of Chebyshev polynomials along the radial grid and on a Fourier basis in the (local) vertical direction characterized by the vertical wavenumber k_z. We solve equations (9)–(14) as a linear eigenvalue problem using Dedalus,[1] an open-source pseudo-spectral code (Burns et al. in preparation) . Recall that a linear eigenvalue problem in one dimension has the general form:

$$\mathcal{M}(r)\boldsymbol{\xi}(r) = \omega \mathcal{I} \boldsymbol{\xi}(r), \tag{45}$$

where $\omega = \omega_R + i\omega_I$ is the complex eigenvalue, $\mathcal{I}$ the identity operator, $\mathcal{M}(r)$ the MHD linear differential operator and $\boldsymbol{\xi}(r)$ the eigenfunction constituted of the perturbed variables in the system. According to our convention for the perturbations given by equation (19), the growth rate of an unstable mode is given by ω_I, such that modes having $\omega_I > 0$ are unstable and those having $\omega_I \leq 0$ are stable. The presence of a non-zero real part ω_R is an indication of the overstability of the mode. Note that although $\omega_R = 0$ implies a non-propagating mode, a non-zero $\omega_R = 0$ need not necessarily result in a travelling mode, which in fact requires a non-zero group velocity.

Note that Dedalus does not allow overspecification of the boundary conditions and, hence, one needs to supply exactly as many boundary conditions as there are first-order, independent Chebyshev derivatives (which in our case is ∂_r only). For the axisymmetric problem defined above, this number is four. We choose rigid (or hardwall) radial boundary conditions such that

$$v_{1r} = 0 \quad \text{at} \quad r = R_{in}, R_{out}$$

$$\partial_r B_{1z} = 0 \quad \text{at} \quad r = R_{in}, R_{out}, \tag{46}$$

where the second condition is motivated by Kersalé et al. (2004).

We choose our fiducial case to have a resolution of $N_r = 150$, where N_r is the number of radial grid points, and a wide annulus such that $R_{in} = 1$ and $R_{out} = 5$. A few higher resolution runs, having $N_r = 200$ and 256, were also conducted as required (see Section 5.2.1 below). We briefly mention here how we eliminate numerically spurious eigenvalues, which may creep in due to the truncation of the Chebyshev polynomial series at a finite N_r. We essentially solve the eigenvalue problem at two different resolutions, N_r and $1.5N_r$, and retain only those modes which are the same between the two resolutions for an assigned tolerance (see e.g. Boyd 2001). This ensures that the solutions are well resolved.

We also constructed solutions for a narrow annulus such that $R_{in} = 1$ and $R_{out} = 1.5$, with resolutions $N_r = 64$ and 128. However, the results of the narrow case were only in partial accord with those of the wide case. Recall that the *most* unstable modes in standard weak-field MRI are *all* known to be localized close to the inner radial boundary in global analyses (Curry et al. 1994; Latter et al. 2015). However, in the presence of a suprathermal toroidal field, the most unstable modes of the system behave very differently and only *some* of them are localized close to the inner radius, whereas others span a wider radial extent (as discussed in Section 5.2.2). Thus, the narrow case solutions agree with

[1] Dedalus is available at http://dedalus-project.org.

only those wide case solutions that are localized towards the inner radial boundary. We present here the results for the wide annulus only, with the aim of extracting the complete global picture. In order to confirm that our fiducial annulus of $r \in [1, 5]$ is indeed adequate to capture all the global solutions, we also conducted a few calculations using a wider annulus of $r \in [1, 7]$ and $N_r = 256$. We found that the results of the two cases were in excellent agreement.

We mention in this context that we also solved the eigenvalue problem using the method described in appendix A of Béthune, Lesur & Ferreira (2016), which again uses a pseudo-spectral representation based on Chebyshev polynomials in the radial direction and a Fourier basis in the vertical direction. We found these results to be in good accord with those obtained from Dedalus, however, we present here only the latter due to its comparatively wider scope.

4.2 Normalization scheme

In order to non-dimensionalize our original dimensionful, linearized equations (9)–(14) for the global analysis, we use quantities at the inner radial boundary $R_{in} = 1$. We scale all frequencies by the inner Keplerian frequency Ω_{in} and all velocities (including Alfvén velocities) by the inner Keplerian velocity v_{in}, which are essentially, $\Omega_{in} = v_{in} = \sqrt{GM} = 1$; all length-scales by $R_{in} = 1$; all wavenumbers by $1/R_{in}$ and all densities by the constant background density $\rho_0 = 1$. We also assume an adiabatic background such that equation (18) holds true with a constant sound speed c_s. We consider the exact background equilibrium given by equation (43), which when non-dimensionalized according to this scheme becomes

$$\Omega = r^{-3/2}(1 + r v_{A\phi}^2)^{1/2}, \tag{47}$$

where $v_{A\phi}$ now represents the dimensionless background toroidal Alfvén velocity. Thus, the final set of dimensionless, axisymmetric, linearized equations that we solve is

$$-i\omega\rho_1 + \partial_r v_{1r} + \frac{1}{r}v_{1r} + ik_z v_{1z} = 0, \tag{48}$$

$$-i\omega v_{1r} - 2r^{-3/2}(1 + r v_{A\phi}^2)^{1/2} v_{1\phi} + c_s^2 \partial_r \rho_1 - v_{A\phi}^2 \frac{\rho_1}{r} + v_{A\phi}\partial_r v_{A1\phi} + v_{Az}\left(\partial_r^2 a_{1\phi} + \frac{1}{r}\partial_r a_{1\phi} - \frac{a_{1\phi}}{r^2} - k_z^2 a_{1\phi}\right) + \frac{2}{r}v_{A\phi}v_{A1\phi} = 0, \tag{49}$$

$$-i\omega v_{1\phi} + \frac{1}{2}r^{-3/2}(1 + r v_{A\phi}^2)^{1/2} v_{1r} + \frac{1}{2}r^{-1/2} v_{A\phi}^2 (1 + r v_{A\phi}^2)^{-1/2} v_{1r} - ik_z v_{Az} v_{A1\phi} + \frac{1}{r}ik_z v_{A\phi} a_{1\phi} = 0, \tag{50}$$

$$-i\omega v_{1z} + ik_z c_s^2 \rho_1 + ik_z v_{A\phi} v_{A1\phi} = 0, \tag{51}$$

$$\omega k_z a_{1\phi} + ik_z v_{Az} v_{1r} = 0, \tag{52}$$

$$-i\omega v_{A1\phi} - ik_z v_{Az} v_{1\phi} - \frac{3}{2}r^{-3/2}(1 + r v_{A\phi}^2)^{1/2} ik_z a_{1\phi} + \frac{1}{2}r^{-1/2} v_{A\phi}^2 (1 + r v_{A\phi}^2)^{-1/2} ik_z a_{1\phi} + v_{A\phi}(\partial_r v_{1r} + ik_z v_{1z}) = 0, \tag{53}$$

where,

$$v_{A1\phi} = \frac{B_{1\phi}}{\sqrt{(4\pi\rho_0)}}\left(\frac{1}{v_{in}}\right), \tag{54}$$

$$a_{1\phi} = \frac{A_{1\phi}}{\sqrt{(4\pi\rho_0)}}\left(\frac{1}{v_{in} R_{in}}\right) \tag{55}$$

and v_{Az} is the dimensionless vertical Alfvén velocity.

The eigenfunctions $\boldsymbol{\xi}(r)$, from equation (45), for the above problem are then given by $\{\rho_1, v_{1r}, v_{1\phi}, v_{1z}, v_{A1\phi}, a_{1\phi}\}$. Note that all the variables appearing henceforth in this work (i.e. in both the global eigenvalue solutions and the PLUTO simulations) are non-dimensionalized according to scheme explained in this section.

5 GLOBAL SOLUTIONS

Here, we present the solutions of the global eigenvalue problem defined by equations (48)–(53). Note that *both* the global and local solutions include the effects of magnetic curvature and compressibility, while ignoring all background gradients except for the radially varying angular velocity. Following PP05, we fix the dimensionless sound speed at $c_s = 0.05$ and the dimensionless vertical Alfvén velocity at $v_{Az} = 0.01$, and compute solutions for different values of (constant) dimensionless toroidal Alfvén velocity $v_{A\phi}$, focusing on the suprathermal cases such that $c_s < v_{A\phi} < 1$ (we discuss the meaning of the upper limit on $v_{A\phi}$ in Section 5.2.1).

Note that a reduction in the growth rate of MRI is expected to occur with the increase of the background toroidal field strength, as has been shown in weak-field studies even in the absence of magnetic curvature (Blaes & Balbus 1994). What PP05 were interested in is any other change in behaviour due to the inclusion of curvature, albeit in a local framework, whereas we are interested to see if their findings hold true in a global framework.

5.1 PP05 stability criteria

Before laying out our results, we briefly recall the instability criteria obtained by PP05 from their approximate local analysis, as a guideline for our comparison study. Equations (47) and (48) of PP05 give the critical wavenumbers bounding the different suprathermal instabilities shown in fig. 5 of PP05 such that

$$(k_{c1} v_{Az})^2 = 3 \tag{56}$$

and

$$(k_{c2} v_{Az})^2 = \frac{v_{A\phi}^4}{c_s^2} - 1, \tag{57}$$

recalling again that PP05 considered a purely Keplerian background equilibrium flow with a dimensionless epicyclic frequency $\kappa = 1$ to obtain these relations. Note that the criterion given by equation (56) is the classic Balbus–Hawley criterion for MRI to operate in a Keplerian flow (Balbus & Hawley 1991), and for $v_{Az} = 0.01$, this yields $k_{c1} \approx 173$. The existence of these critical wavenumbers thus sets the stabilization scale for the instabilities in the suprathermal regime. We note here that the various critical wavenumbers derived by PP05 are only approximate and their exact values would depend on the full global solution of the linearized MHD equations. Additionally, the critical wavenumber that limits MRI in the global analysis would no longer remain a constant but would depend on the background toroidal field. Hence, from now onwards, we refer to the maximum allowed vertical wavenumber for MRI to occur in the global analysis as k_{MRI} for simplicity (note that in the approximate local analysis of PP05, $k_{MRI} \equiv k_{c1}$).

According to PP05, setting the right-hand side of equation (57) above to zero yields the critical value for the suprathermal Alfvén speed above which MRI *starts* to get stabilized for the smallest wavenumbers, i.e. $v_{A\phi}^{PP1} = \sqrt{c_s}$. Consequently, setting the right-hand sides of equations (56) and (57) equal to each other yields the critical value at which MRI is *completely* stabilized for all wavenumbers, namely, $v_{A\phi}^{PP2} = \sqrt{2c_s}$. For $c_s = 0.05$, these limits become $v_{A\phi}^{PP1} \approx 0.22$ and $v_{A\phi}^{PP2} \approx 0.32$.

Keeping this general picture in mind, we will now proceed to verify to what degree our global solutions agree with the local predictions.

5.2 Numerical eigenvalue analysis

5.2.1 Suprathermal instabilities

We begin by showing the global eigenvalue solutions for the standard weak-field MRI case ($v_{A\phi} = 0$) as a reference for the suprathermal cases ($v_{A\phi} > c_s$) to follow. In order to estimate the associated plasma β of our cases, we recall that $\beta = P/P_B = 8\pi P/(B_\phi^2 + B_z^2)$. If we consider $P = \rho c_s^2$, then we can write $\beta = 2c_s^2/(v_{A\phi}^2 + v_{Az}^2)$. Thus, for $v_{Az} = 0.01$ and $c_s = 0.05$, the case with $v_{A\phi} = 0$ has $\beta = 50 \gg 1$, while the cases with $v_{A\phi} = 0.1, 0.25, 0.3, 0.4$, have $\beta = 0.5, 0.08, 0.06, 0.03 < 1$ respectively.

In Fig. 1, we plot the imaginary part ω_I of the eigenvalues as a function of the vertical wavenumber k_z, indicating all the unstable modes for $v_{A\phi} = 0$ (left-hand panel). We also plot the corresponding real part ω_R of all the modes (right-hand panel), which is an indicator of the overstability of a mode. Note that a global problem exhibits a large family of modes as seen in Fig. 1. Thus, each value of k_z corresponds to multiple modes and the mode with the *maximum* growth rate is the *most* unstable mode at that k_z. The locus connecting the maximum growth rate modes at different k_z demarcates the set of *most* unstable modes of the system, which is indicated by the cyan line in the left-hand panel of Fig. 1. The cyan line in the right-hand panel of Fig. 1 denotes the ω_R corresponding to the *most* unstable modes.

We see from Fig. 1 that the maximum possible growth rate for standard MRI in the global analysis is about 0.67, which is less than but comparable to the local prediction of 0.75 (Balbus & Hawley 1998), as also observed in previous global studies (see e.g. Curry et al. 1994; Latter et al. 2015). The corresponding phase velocities of the most unstable modes are exactly zero, which also matches the local theory, as MRI is known to be a purely unstable mode with a non-propagating character. We note from Fig. 1 that $k_{MRI} \approx 160$, i.e. less than the local prediction of ∼173 (see Section 5.1). In the right-hand panel of Fig. 1, we also demarcate the bands of fast magnetosonic, Alfvén and slow magnetosonic modes, indicated by the red letters F, A and S, respectively. This is to better understand the nature of the *new* suprathermal instabilities – just like in the case of standard MRI, which is known to be a destabilized slow mode. In this context, we mention that for standard weak-field MRI, the global problem has a dispersion relation that happens to be identical in form to that in the local problem (Latter et al. 2015). This explains the excellent agreement between the local and the global solutions in this case.

One of the goals of the current work is to study the evolution of the *most* unstable modes of the system as the background toroidal field becomes suprathermal, the results of which are summarized by Figs 2 and 3. Fig. 2 compares the growth rate ω_I as a function of k_z obtained from the *global* eigenvalue solutions (left-hand panels) of the axisymmetric equations (48)–(53) with that obtained from the solutions of the *local* dispersion relation (right-hand panels) given by equation (44) for a constant radial wavenumber $l = 10$, for different suprathermal $v_{A\phi}$. This choice of l satisfies the WKB constraint (see Section 3.1) and, also, ensures that the value of l^2/k_z^2 remains small for a large range of k_z, which is essentially the PP05 limit we want to compare our global results with. Fig. 3 shows the real part of the eigenvalues ω_R as a function of k_z for the same cases as in Fig. 2. Note that we mainly compare the *most* unstable modes (denoted by cyan lines) between the left- and right-hand panels (or PP05 case) of these two figures. We list the main results of this section below:

(i) At a glance, we observe that the *maximum* growth rates for different $v_{A\phi}$ appear to be similar between the left- and right-hand panels of Fig. 2, with the latter slightly overestimating the growth rates in general (except for $v_{A\phi} = 0.4$, as we note below). The ω_R of the most

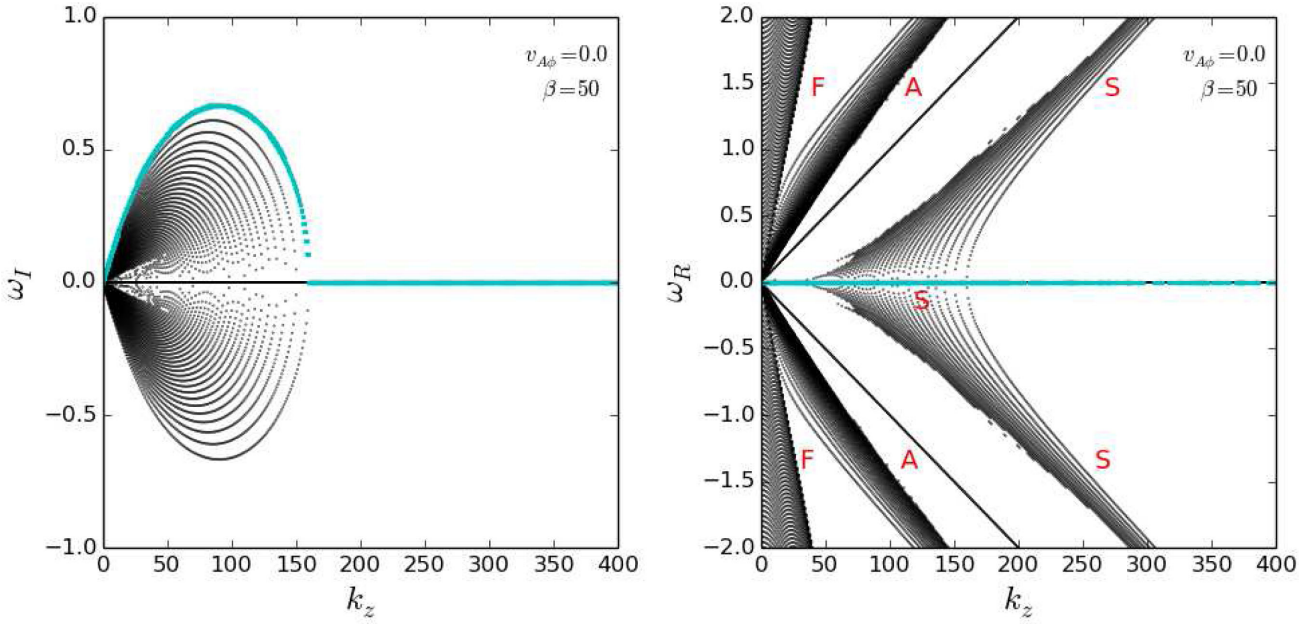

Figure 1. Global eigenvalue solutions for standard MRI (i.e. $v_{A\phi} = 0$). Left-hand panel: the imaginary part ω_I of the modal frequency, or, the growth rate of all the unstable modes, as a function of k_z. Right-hand panel: the real part ω_R of the modal frequency as a function of k_z. The cyan line in both panels demarcates the most unstable modes for this case. The letters F, S and A denote the fast, slow and Alfvén modes, respectively. The background accretion flow has $c_s = 0.05$ and $v_{Az} = 0.01$, and the global problem is solved on a radial grid $r \in [1, 5]$ with resolution $N_r = 150$.

unstable modes (cyan line) also looks similar between the left- and right-hand panels of Fig. 3. Additionally, we observe that the band of fast modes indeed lie decoupled from the rest of the modes in the global case, thus justifying our assumption of neglecting them in Section 3.1. However, as $v_{A\phi}$ increases, the global and local solutions start differing in the vertical wavenumber occupancies of the most unstable modes. Note from Fig. 2 that we do not observe any modes growing on arbitrarily short scales as PP05 find for a finite l/k_z, either in our local or global solutions, as discussed in Section 3.3.

(ii) For $v_{A\phi} = 0.25$, which is slightly greater than the first PP05 limit ($v_{A\phi}^{PP1} \sim 0.22$), the most unstable modes in the global case exhibit a low growth rate tail extending all the way to $k_z = 0$, unlike in the corresponding PP05 case, which shows complete MRI stabilization at low k_z. The ω_R of the most unstable modes in the global case also extends all the way to $k_z = 0$. In order to ensure that this result is not an artefact of inadequate resolution, we verified it using two higher resolutions, $N_r = 200$ and 256.

(iii) When $v_{A\phi} = 0.3$, i.e. close to the second PP05 limit ($v_{A\phi}^{PP2} \sim 0.32$), we observe a drastic suppression of the MRI growth rate in the global case, to only a few per cent of the maximum growth rate for standard MRI (compare with the left-hand panel of Fig. 1), as predicted by PP05. Thus, there indeed seems to be a threshold $v_{A\phi}$ for MRI to operate. However, even at this stage, the instability extends all the way to the smallest vertical wavenumbers (as displayed by the corresponding cyan lines in the global case of Figs 2 and 3). This is contrary to the PP05 case where the MRI is suppressed across almost the entire range of allowed wavenumbers. The global result was further verified using two higher resolutions of $N_r = 200$ and 256.

(iv) When the toroidal field strength increases further, there seems to be the appearance of two new instabilities for $v_{A\phi} = 0.4$, in the local as well as the global analysis. We note here that although PP05 mention the origin of the two new instabilities 'as the result of coupling between the modes that become the Alfvén and the slow modes in the limit of no rotation', this does not provide a very clear insight into the exact nature of these instabilities. We attempt to resolve this issue here.

Recalling from the right-hand panels of Fig. 2, the instability in the region $k_{c1} < k_z \leq k_{c2}$ was termed instability II by PP05, which they claimed to be a generalization of the axisymmetric toroidal buoyancy mode proposed by Kim & Ostriker (2000). The instability that emerges in a *limited* range $0 < k_z < k_{c1}$, was termed instability III by PP05 (see Section 5.1 for the definitions of the various critical wavenumbers). Now, if we track the slow modes as $v_{A\phi}$ increases down the right-hand panels of Fig. 3, we note from the bottommost panel that instability II of PP05 seems to arise due to a destabilization of the same slow modes that give rise to MRI. However, since this instability appears only for suprathermal magnetic fields $v_{A\phi} > 0.3$, we refer to it with the more physically motivated name of 'suprathermal slow mode instability (SSMI)'. This slow mode is denoted by the letter S in the bottommost right panels of Figs 2 and 3. Similarly, if we track the Alfvén modes along with the slow modes, we notice a merging of these two modes in the bottommost right panel of Fig. 3, in a limited wavenumber range $0 < k_z < k_{c1}$. This merging indicates the loss of the individual identities of the slow and Alfvén modes and the emergence of a hybrid unstable mode. This mode is labelled with an H in the bottommost right panels of Figs 2 and 3. We refer to it as the 'suprathermal hybrid mode instability (SHMI)' instead of instability III, in order to convey its physical origin. If we track the band of slow and Alfvén modes down the left-hand panels of Fig. 3, we see that the same deduction is applicable in the global case as well (for the most unstable modes). In this

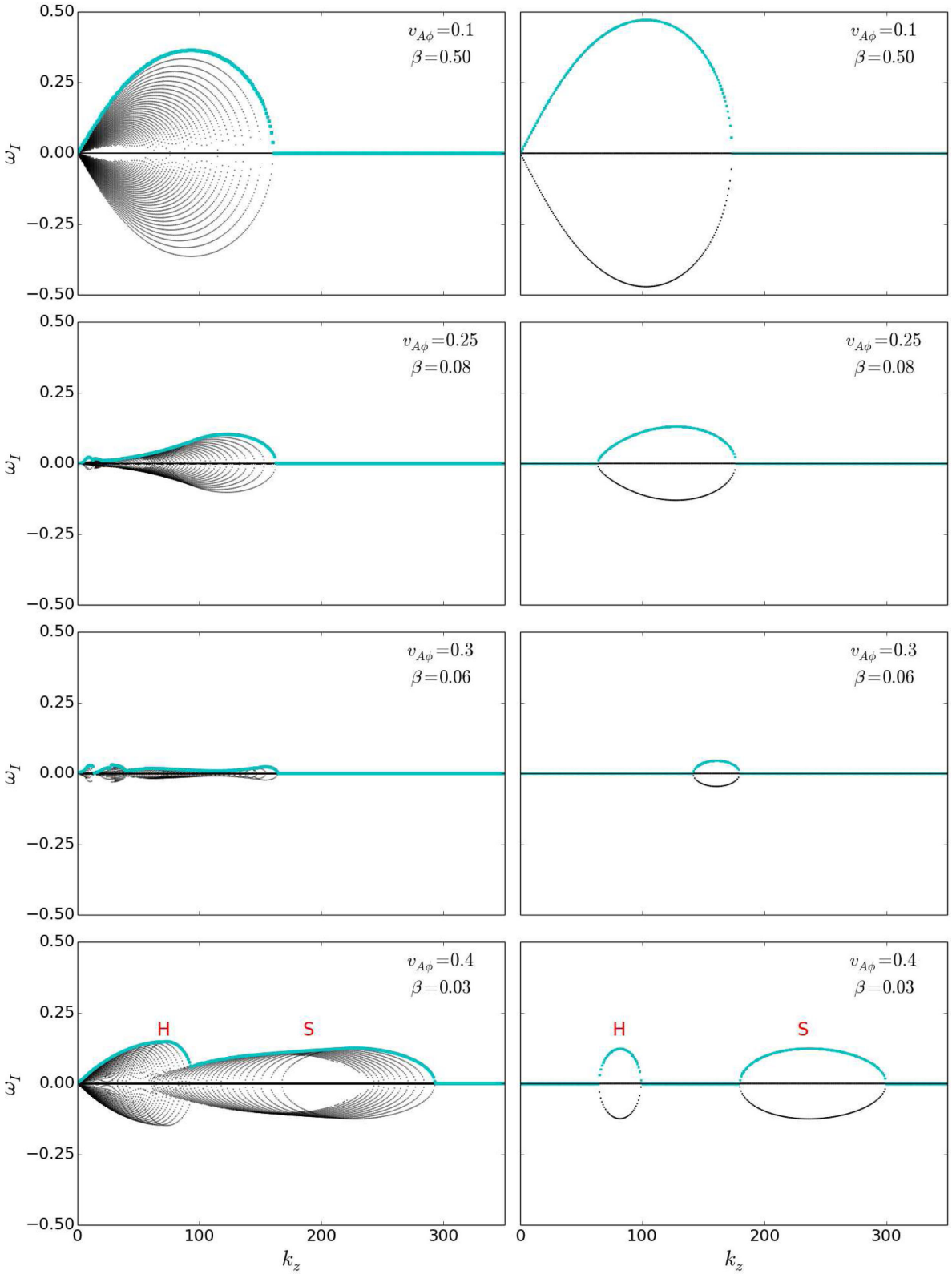

Figure 2. The growth rate $\omega_{\rm I}$ of the unstable modes as a function of k_z for different suprathermal $v_{{\rm A}\phi}$ and $\beta < 1$. Left-hand panel: global eigenvalue solutions. Right-hand panel: solutions of the local dispersion relation given by equation (44) with $l = 10$. The cyan line in all the panels demarcates the most unstable modes for the corresponding $v_{{\rm A}\phi}$. The letters H and S denote hybrid and slow modes, respectively. The background accretion flow has $c_{\rm s} = 0.05$ and $v_{\rm Az} = 0.01$, and the global problem is solved on a radial grid $r \in [1, 5]$ with resolution $N_{\rm r} = 150$.

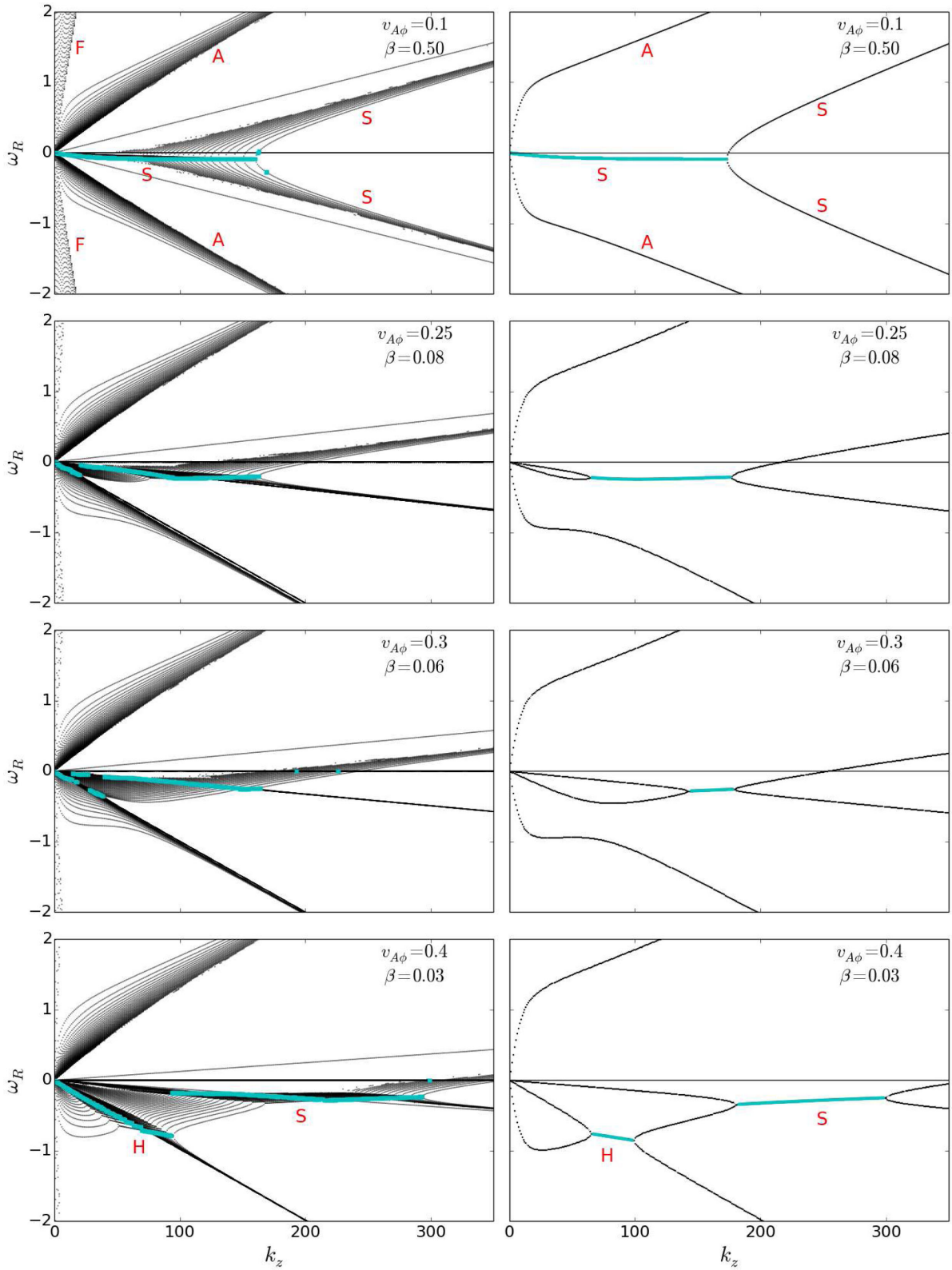

Figure 3. The real part ω_R of the modal frequency as a function of k_z for different suprathermal $v_{A\phi}$ and $\beta < 1$. The left- and right-hand panels represent the same cases as the left- and right-hand panels of Fig. 2. The letters F, S, A and H denote the fast, slow, Alfvén and hybrid modes, respectively. The cyan line in all the panels denotes the ω_R corresponding to the most unstable modes for the corresponding $v_{A\phi}$. The background accretion flow has $c_s = 0.05$ and $v_{Az} = 0.01$, and the global problem is solved on a radial grid $r \in [1, 5]$ with resolution $N_r = 150$.

context, we mention that Blaes & Socrates (2001) also studied the interplay of various Alfvénic, slow- and fast-mode instabilities, however, only in weakly magnetized, radiation pressure dominated accretion discs.

(v) We observe, however, a few differences between the local and global solutions for $v_{A\phi} = 0.4$.
Both SSMI and SSMI have roughly the same maximum growth rate for $v_{A\phi} = 0.4$ in the local case. However, in the global case, the maximum growth rate of SHMI is slightly higher than that of SSMI. Also, in the global case, SHMI extends all the way to $k_z = 0$ unlike in the PP05 case. This seems to point to the fact that SHMI is the mode that replaces MRI beyond the second PP05 limit. Next, there seems to be an overlap between the *most* unstable modes (cyan line) of SHMI and SSMI in the $\omega_I - k_z$ plane. The growth rate of the most unstable modes of SHMI drops at $k_z \sim 93$ but rises again, and smoothly gives way to the most unstable modes of SSMI well before going to zero. This is in direct contrast with the corresponding PP05 case, where SHMI gets completely stabilized at $k_z \sim 100$ before SSMI appears at a distinctly higher k_z (see bottommost right panel of Fig. 2). However, we observe a clear discontinuity in the $\omega_R - k_z$ plane at $k_z \sim 93$ for the *most* unstable modes (cyan lines) in the global case of Fig. 3. This establishes that SHMI and SSMI are not the same but distinct instabilities, having different origins, different phase velocities and occupying different wavenumber regimes.

(vi) We summarize here the different critical wavenumbers that emerge from the global analysis in the suprathermal regime (as seen in the left-hand panels of Figs 2 and 3). Note that for all $v_{A\phi} \lesssim 0.3$, the maximum allowed vertical wavenumber for the instability is still given by k_{MRI} (in accordance with the Balbus–Hawley instability criterion) and MRI, although suppressed, occupies the *entire* range $0 \leq k_z \leq k_{MRI}$.

With a further increase in $v_{A\phi}$, two new critical wavenumbers emerge. The larger of the two critical wavenumbers is the maximum allowed wavenumber for SSMI, which matches reasonably well with that predicted by PP05, namely, k_{c2} given by equation (57). Thus, SSMI does not keep growing indefinitely with increasing k_z in the global case but stabilizes at a well-defined short scale. We term the smaller critical wavenumber k_{SI} (where SI stands for suprathermal instability), which denotes the point of discontinuity in the $\omega_R - k_z$ plane for the most unstable modes when $v_{A\phi} = 0.4$. This demarcates *both* the maximum allowed wavenumber for SHMI as well as the minimum onset wavenumber for SSMI. (Note that k_{SI} is a characteristic of only the *most* unstable SHMI and SSMI modes, unlike k_{c2}, which denotes the maximum limit for *all* SSMI modes.) Interestingly, unlike k_{c2}, the critical wavenumber k_{SI} does not have a local analogue. Thus, the most unstable modes of SHMI lie in the wavenumber range $0 \leq k_z \leq k_{SI}$, whereas those of SSMI occupy the wavenumber range $k_{SI} \leq k_z \leq k_{c2}$ in the global case. We mention here that with increasing $v_{A\phi}$, the maximum growth rates of both SHMI and SSMI increase. These two instabilities also expand their respective wavenumber occupancies, such that both k_{SI} and k_{c2} increase with an increase in $v_{A\phi}$. The fact that in the global case, SHMI and SSMI coexist for the same $v_{A\phi}$, overlap in the $\omega_I - k_z$ plane and span a large wavenumber range between them, might have important implications for energy exchange between these modes in the non-linear regime.

(vii) We briefly discuss in this context how the LFI of Curry & Pudritz (1995) compares with the new suprathermal instabilities obtained in this work.

The LFI is a single instability that appears after MRI stabilization in an *incompressible* flow having a shear parameter $q \neq 2$, for $v_{A\phi}$ *greater* than the rotational speed. The SHMI and SSMI on the other hand are two distinct instabilities, which appear and coexist after MRI stabilization in a *compressible* flow for suprathermal $v_{A\phi}$*less* than the rotational speed. The maximum growth rate and vertical wavenumber occupancy of LFI increase with $v_{A\phi}$ (see fig. 5 of Curry & Pudritz 1995), which is similar to the behaviour of SHMI and SSMI mentioned above. Both LFI and SHMI (in the global case) have growth rates extending all the way to $k_z = 0$ (in contrast with the local prediction). Thus, SHMI and SSMI together can be thought of as the compressible counterpart of LFI.

(viii) An important point to note here is that although our current analysis is cylindrical and vertically unstratified, in a realistic disc k_z cannot be arbitrarily small as it is limited by the disc thickness. Following the convention in Balbus & Hawley (1998), we assume the vertical scaleheight of the disc to be $H = \sqrt{2}c_s$ (in our dimensionless units). Moreover, at least one wavelength of the unstable mode must fit within a disc thickness of $2H$. Thus, instability requires $\lambda = 2\pi/k_z < 2H$ or $k_z H > \pi$. On using $c_s = 0.05$, we get a lower limit on k_z such that $k_z \gtrsim 45$ is the physically allowed regions for instability.
We now interpret what it means when the above restriction is applied to the global solutions in Figs 2 and 3. Even when the low-k_z zone is discarded, the suppression of MRI with increasing suprathermal $v_{A\phi}$ is still relevant as it occurs at all k_z, and this effect should be captured in global, vertically stratified simulations. However, when $v_{A\phi}$ is increased beyond MRI stabilization, a significant portion of the low-k_z region occupied by SHMI becomes unphysical (as seen from the bottommost left panel of Fig. 2), while SSMI remains largely unaffected. Nevertheless, SHMI can operate in the range $45 < k_z \lesssim 93$ (for $v_{A\phi} = 0.4$) and, hence, might still be a physical instability. Moreover, with a further increase in $v_{A\phi}$, SHMI expands its wavenumber occupancy and, hence, can occupy larger physically allowed regions.

(ix) We find that the most unstable modes of *all* the suprathermal instabilities (i.e. for all $v_{A\phi} \geq 0.1$) are overstable, having non-zero ω_R in both the local and global cases (unlike in standard MRI), as seen in Fig. 3. Depending on the relative magnitudes of ω_I and ω_R, the unstable modes could be predominantly amplified, if $|\omega_I| > |\omega_R|$ or predominantly oscillatory, if $|\omega_I| < |\omega_R|$. The group velocity of the most unstable modes in the global case can be estimated numerically from the left-hand panels of Fig. 3, such that $v_{gr} = \partial\omega_R/\partial k_z$. A non-zero v_{gr} would imply that these unstable modes travel vertically across the disc. The distance travelled by an unstable mode in unit growth time is given by $\Delta z = |v_{gr}|/|\omega_I|$ (note that both v_{gr} and Δz are functions of k_z). However, in order to estimate how large Δz is, we have to compare it with H (for $c_s = 0.05$, $H \sim 0.07$). For example, for $v_{A\phi} = 0.1$, we obtain $0 \leq |v_{gr}| \lesssim 0.002$ and $0 \leq \Delta z \lesssim 0.02$ for the unstable MRI mode. For $v_{A\phi} = 0.4$, we obtain $0.005 \lesssim |v_{gr}| \lesssim 0.02$ and $0.02 \lesssim \Delta z \lesssim 0.05$ for SHMI, and $0 \leq |v_{gr}| \lesssim 0.001$ and $0 \leq \Delta z \lesssim 0.01$ for SSMI. Since $\Delta z < H$ in all cases, this implies that these modes probably do not propagate far enough, in unit growth time, to invalidate a local analysis along the vertical direction.

(x) We take a moment here to briefly discuss the meaning of the upper limit on $v_{A\phi}$ maintained in this work. The non-Keplerian background angular velocity in our work has a rotational component that decreases with radius, as well as a magnetic component that is constant. The limit $v_{A\phi} < 1$ means, in our units, that the toroidal Alfvén velocities are chosen such that they are always less than the Keplerian velocity at the inner radius $R_{in} = 1$, i.e. $v_{A\phi} < v_{in} = 1/\sqrt{R_{in}}$. This ensures that the *inner* disc is always rotationally supported (i.e. the rotational component is larger than the magnetic component in the background flow). A more stringent upper limit, to ensure that the *entire* disc is rotationally supported, is given by $v_{A\phi} < 1/\sqrt{R_{out}}$, which for our fiducial case with $R_{out} = 5$ implies that $v_{A\phi} < 0.45$ should be satisfied. If $v_{A\phi} > 1/\sqrt{R_{out}}$, then it means the outer portion of the disc is magnetically supported, which might affect the unstable modes of the system differently.

Since our aim in this work is to compare directly with the results of PP05, we fixed $c_s = 0.05$ and $v_{Az} = 0.01$ following them, but restricted our suprathermal results to $v_{A\phi} = 0.4$ to ensure a fully rotationally supported disc. However, one can repeat the analysis for a smaller c_s (and a suitably smaller v_{Az} to ensure it is subthermal), in order to explore the effect of a wider range of suprathermal $v_{A\phi} < 1$, without treading the uncertain regime of magnetically supported discs. Hence, we also carried out the global analysis using $c_s = 0.01$ and $v_{Az} = 0.005$, the results of which are qualitatively similar to those in Figs 2 and 3. The critical fields for MRI suppression are lower and in accordance with equations (56) and (57), such that $v_{A\phi}^{PP1} \sim 0.1$ and $v_{A\phi}^{PP2} \sim 0.14$, and the vertical wavenumbers span a wider range due to a smaller v_{Az}.
We encountered an interesting difference between the local and global solutions when performing the analysis with a different c_s. In the *local* case, $v_{A\phi}^{PP2}$ demarcates both the complete stabilization of MRI as well as the onset of SSMI, however, SHMI appears at a slightly higher $v_{A\phi}$, let us call it $v_{A\phi}^{PP3}$ (which has no analytical criteria and needs to be determined numerically). As c_s decreases, the separation between $v_{A\phi}^{PP2}$ and $v_{A\phi}^{PP3}$ keeps increasing. In the *global* case, on the contrary, SHMI and SSMI always appear together, right after the suppression of MRI at $\sim v_{A\phi}^{PP2}$.

5.2.2 *Global eigenfunctions and eigenspectra*

A very important benefit of the global problem over a local analysis is that it allows us to study the global eigenfunctions of the problem. In this section, we study the radial eigenfunctions for a *fixed* k_z and *different* $v_{A\phi}$. We also look at the complete eigenspectra of all the modes (both stable and unstable), again for a fixed k_z and different $v_{A\phi}$.

In the left-hand panels of Fig. 4, we show the eigenspectrum of all the modes in the $\omega_R - \omega_I$ plane, for different suprathermal $v_{A\phi}$ at a fixed $k_z = 90 < k_{SI} \approx 93$. The red dot denotes the *most* unstable mode at this k_z. In the right-hand panels of Fig. 4, we plot three normalized eigenfunctions corresponding to the most unstable mode at $k_z = 90$ (i.e. the red dot in the left-hand panel) as a function of radius. These are $\{\rho_1, v_{1r}, v_{A1\phi}\}$, which are normalized with respect to their respective maximum amplitudes (for the eigenfunctions of standard weak-field MRI, see Latter et al. 2015). Fig. 5 is the same as Fig. 4, except that it is plotted for $v_{A\phi} = 0.4$ at $k_z = 200 > k_{SI} \approx 93$ (we do not show the other cases of Fig. 4, since there is no instability at $k_z = 200$ for $v_{A\phi} < 0.4$). We point out that the instability represented in this case is the SSMI, while that in the bottommost panels of Fig. 4 is SHMI (see Section 5.2.1 for the definition of k_{SI}). The key features to note from Figs 4 and 5 are as follows:

(i) The eigenspectra tell us that if the modes lie exactly on the horizontal axis, they are purely unstable (as in the case of standard weak-field MRI), while if they lie exactly on the vertical axis then they are purely stable. Any modes that lie in between the two axes are overstable. Thus, from the left-hand panels of Figs 4 and 5, we clearly see the overstability of the modes for all the suprathermal cases. As the field becomes more suprathermal, the family of modes seem to form more interesting structures in the $\omega_R - \omega_I$ plane than in the case of standard weak-field MRI. The growth rates of *all* the unstable modes approach zero as $v_{A\phi} \to 0.3$, and again increase for $v_{A\phi} = 0.4$, as already seen from Figs 2 and 3.

(ii) In the right-hand panels, we observe that all three eigenfunctions for a given $v_{A\phi}$ look very similar to each other in terms of their number of nodes as well as radial extent (a node occurs every time a radial eigenfunction crosses zero). We observe that the eigenfunctions of the most unstable mode show different degrees of radial localization for different $v_{A\phi}$. We further note that the greater the number of nodes, the less localized the eigenfunctions tend to be and vice versa. This might be indicative of the potential driving mechanisms behind the most unstable modes in the suprathermal regime (note, however, that this is not fully conclusive because of the lack of energetics in our analysis). The highly radially localized modes are likely to be shear driven, as the differential rotation dominates over the restoring magnetic tension force in the inner regions of the disc. This is the case for standard MRI (see Latter et al. 2015) and also seems to be so for lower field strengths like $v_{A\phi} = 0.1$. On the other hand, the radially extended modes could be possibly driven by radial buoyancy caused by the magnetic tension force of the suprathermal toroidal field, which tends to dominate in the outer regions of the disc.

6 NUMERICAL SIMULATIONS

In this section, we present the results of a small set of numerical simulations that we performed using the finite-volume code PLUTO (Mignone et al. 2007), which solves the fully non-linear equations of ideal MHD. Our motivation is to verify that the suppression of MRI as well as the newly identified suprathermal instabilities can indeed be recovered from numerical simulations of strongly magnetized accretion discs. In this work, we focus on the linear regime only, and defer the non-linear evolution to a future publication.

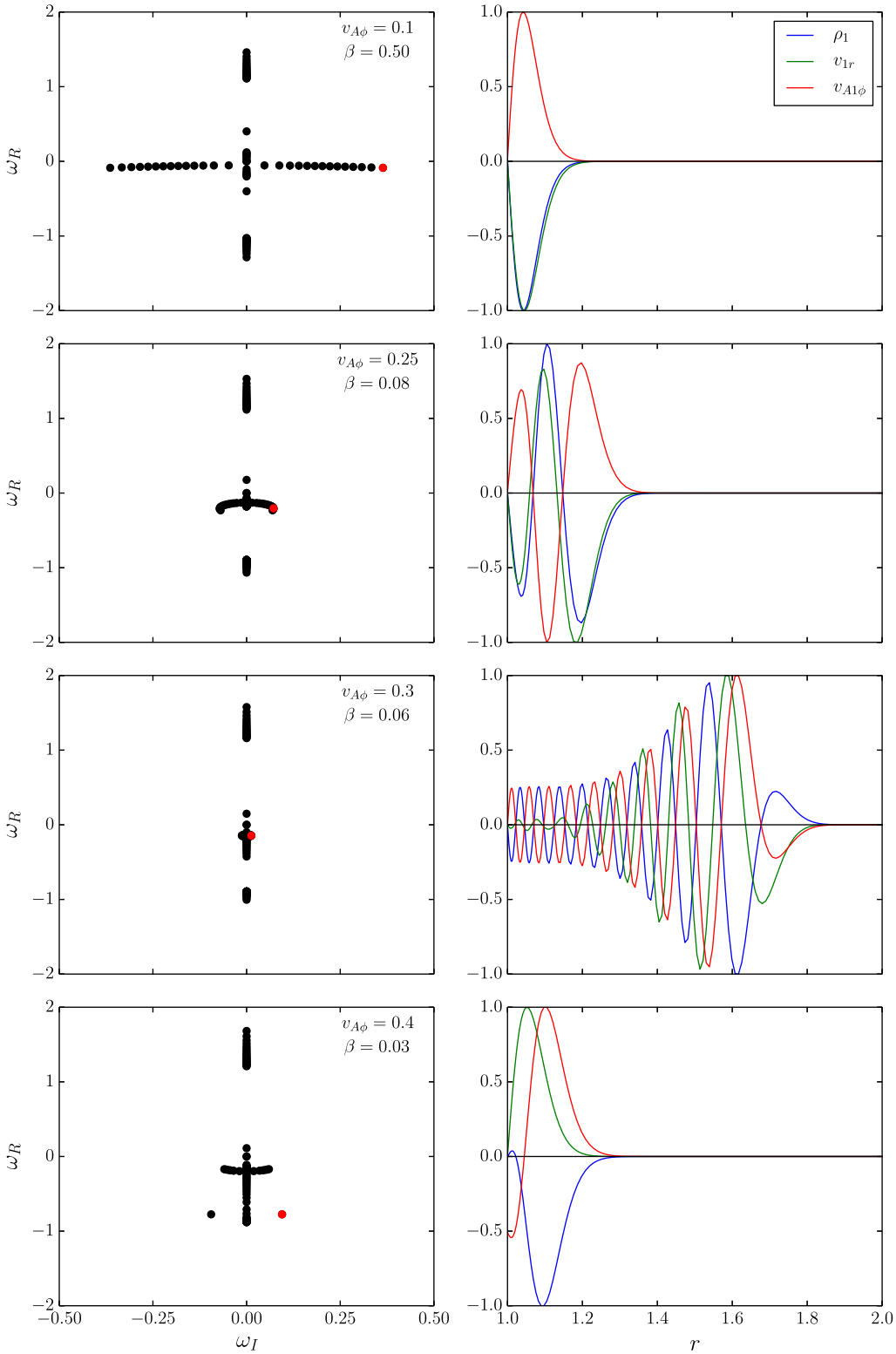

Figure 4. Global properties for different suprathermal cases computed at $k_z = 90$. Left-hand panel: eigenspectrum of all the modes at $k_z = 90$, with the red dot denoting the most unstable mode. Right-hand panel: normalized eigenfunctions for the most unstable mode at $k_z = 90$ as a function of radius r. The background accretion flow has $c_s = 0.05$ and $v_{Az} = 0.01$, and the global problem is solved on a radial grid $r \in [1, 5]$. The grid resolution is $N_r = 150$ for all the left-hand panels, and for the right-hand panels it is $N_r = 256$ for $v_{A\phi} = 0.1$, 0.25, 0.4 and $N_r = 512$ for $v_{A\phi} = 0.3$. Note that the radial axis in the right-hand panel has been zoomed close to the inner boundary.

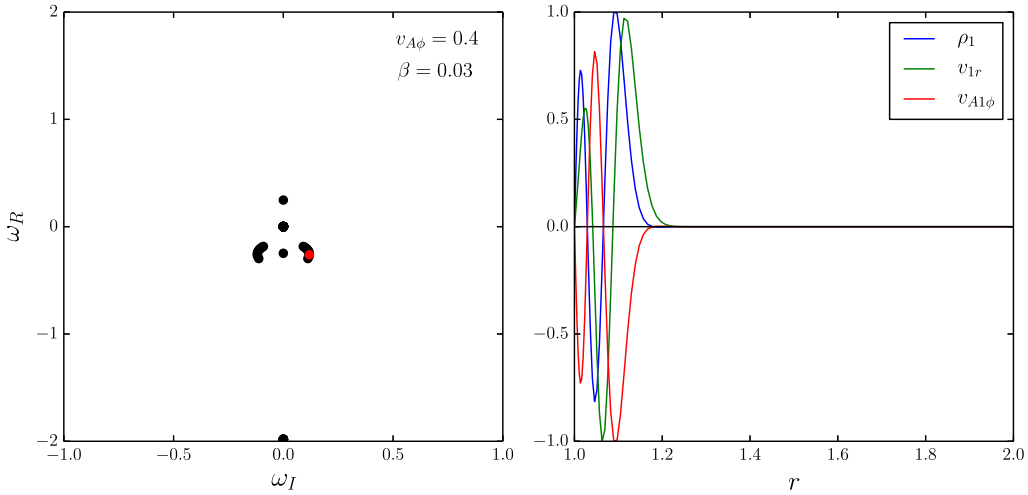

Figure 5. Global properties for $v_{A\phi} = 0.4$ computed at $k_z = 200$. The left- and right-hand panels represent the same properties as in Fig. 4. The background accretion flow has $c_s = 0.05$ and $v_{Az} = 0.01$, and the global problem is solved on a radial grid $r \in [1, 5]$. The grid resolution is $N_r = 150$ for the left-hand panel and $N_r = 256$ for the right-hand panel. Note that the radial axis in the right-hand panels has been zoomed close to the inner boundary.

6.1 Numerical set-up

The numerical set-up we consider matches as closely as possible that of the global linear eigenvalue analysis performed above (see Sections 4 and 5). We work in a 2.5-dimensional (axisymmetric) geometry and consider a grid extending on a (r, z) domain with $r \in [1, 5]$ and $z \in [-0.1, 0.1]$. The radial grid resolution is $N_r = 1536$ and the vertical grid resolution is $N_z = 128$. The boundary conditions are periodic in the vertical direction and outflow in the radial direction, i.e. $v_{1r}(r = R_{in} = 1) = 0$ if $v_{1r}(r = 1^+) < 0$ and $\partial_r v_{1r} = 0$ otherwise. Note that these radial boundary conditions are different than those used for the global eigenvalue analysis (see Section 4.1), which were actually reflective in nature. In spite of this difference, we find that the results of the numerical simulations match quite well with those of the eigenvalue analysis (see Section 6.2 below), indicating that the instabilities we study in this work are independent of the radial boundary conditions. In order to limit numerical diffusion in the presence of suprathermal fields, we use a Roe Riemann solver to compute the intercell fluxes and a third-order Runge–Kutta integration scheme. We use a constrained transport algorithm to ensure $\nabla \cdot \boldsymbol{B} = 0$ at machine precision and reconstruct the electromotive forces using a two-dimensional Riemann solver based on a four-state HLL (Harten-Lax-Van Leer) flux function (Mignone et al. 2007).

We use the inner radius ($r = R_{in} = 1$) of the disc to be the unit of length, and the inverse of the Keplerian frequency at the inner radius (Ω_{in}^{-1}) to be the unit of time in our set-up (note, however, that the disc does not rotate with the Keplerian frequency at the inner radius due to the non-zero background toroidal field). We initialize our simulation with the equilibrium rotation profile given by equation (8), with a uniform mean toroidal and vertical magnetic fields. The flow is assumed to be globally isothermal and has a uniform background density $\rho_0 = 1$. The simulations presented in this section have $v_{Az} = 0.01$ and $c_s = 0.05$. The toroidal Alfvén velocity $v_{A\phi}$ is varied from 0 to 0.6. Finally, we add a global perturbation to the flow with $v_{1r} = 10^{-7} c_s \cos(20r)\cos(k_z z)$, which ensures that only the desired vertical wavenumber is initialized in the numerical set-up (this in turn minimizes contamination due to numerical noise from other scales).

6.2 Linear evolution

We follow the growth of the various instabilities present in this numerical set-up by performing a Fourier transform in the z-direction of the flow at each time-step. In principle, each linearly unstable mode should grow independently and a projection of the flow on each radial linear eigenmode is required to clearly identify the growth rate of each mode. Instead of this, we focus here on the *most* unstable eigenmode for each k_z. This simplifies the characterization of the instabilities since we can then choose one fiducial radius r_{fid} and measure the growth of the norm of the perturbation at this particular radius. An example of such a measure is given in Fig. 6, which shows the norm or, the absolute value, of the Fourier-transformed, perturbed radial magnetic field at a given $k_z = 31$, i.e. $||B_{1r}||$ as a function of time, for $v_{A\phi} = 0.1$. The maximum linear growth rate $\omega_{I\,max}$ that we obtain for this case is 0.19, which agrees quite well with the global eigenvalue analysis, as can be seen when compared with the topmost left panel of Fig. 2 (exact errors given below). In principle, one could choose any perturbed velocity or magnetic field component, and we have checked that the growth rates do not depend on this choice. Note also that in principle, one can choose any r_{fid}. However, choosing a large r_{fid} implies that one has to wait for a long time before the non-growing perturbations have decayed and the most unstable mode shows up. This is because decaying perturbations typically decay on a time-scale $\sim\Omega^{-1}$. Therefore, it is preferable to choose a r_{fid} close to the inner boundary, but not too close to avoid potential effects from the boundary conditions. We have chosen $r_{fid} = 1.05$, which corresponds to 10 grid cells from the inner radial boundary and is sufficient to avoid artefacts from the boundary conditions (using $r_{fid} = 1.1$ did not make any difference to the results).

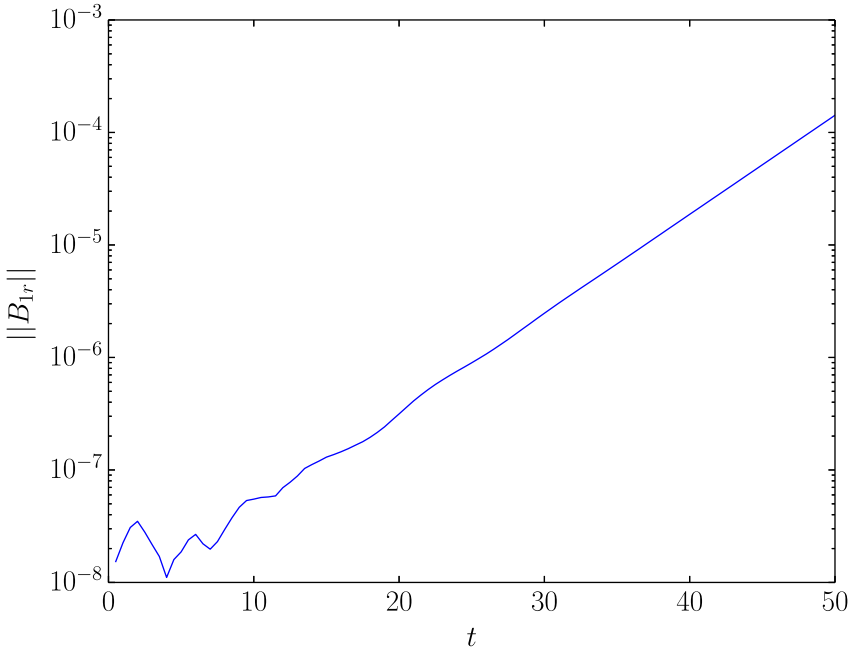

Figure 6. Numerical simulations in PLUTO – norm of the Fourier-transformed perturbation of the radial magnetic field $||B_{1r}||$ as a function of time t, measured at $r_{\rm fid} = 1.05$ for $v_{A\phi} = 0.1$ and $k_z = 31$. Time is in units of $\Omega_{\rm in}^{-1}$ and the measured growth rate in this case is $\omega_{\rm Imax} = 0.19$. The background accretion flow has $c_s = 0.05$ and $v_{Az} = 0.01$, and the simulations are performed on a radial grid $r \in [1, 5]$ and a vertical grid $z \in [-0.1, 0.1]$, with resolutions $N_r = 1536$ and $N_z = 128$, respectively

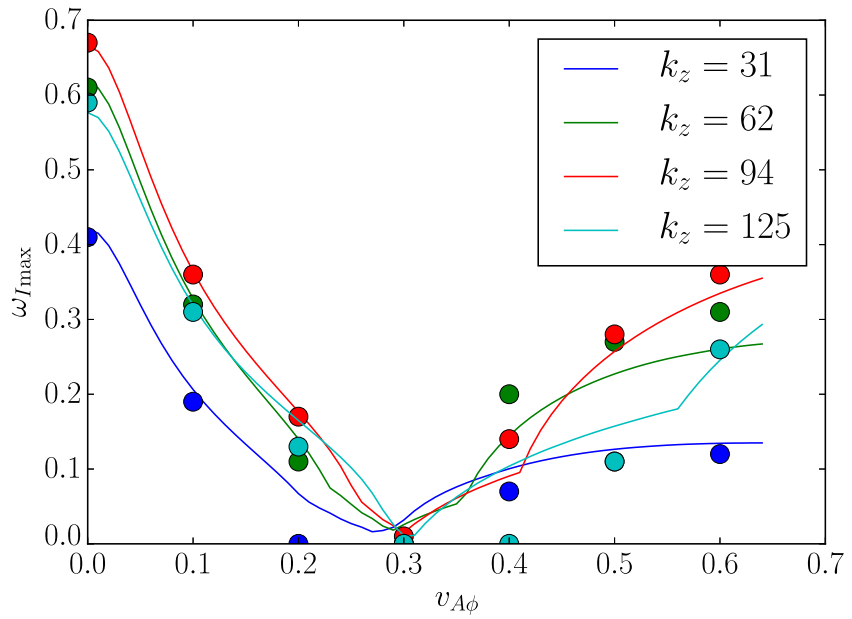

Figure 7. Measured maximum linear growth rates $\omega_{\rm I\,max}$ as a function $v_{A\phi}$ from numerical simulations in PLUTO (filled dots) and predicted growth rates from the global eigenvalue analysis (lines), for the most unstable mode at $k_z = 31$, 62, 94 and 125 (represented by different colours). The background accretion flow has $c_s = 0.05$ and $v_{Az} = 0.01$, and the simulations are performed on a radial grid $r \in [1, 5]$ and a vertical grid $z \in [-0.1, 0.1]$, with resolutions $N_r = 1536$ and $N_z = 128$, respectively.

We have performed several simulations with varying $v_{A\phi}$ to measure the growth rates of the most unstable modes at $k_z = 31$, 62, 94 and 125. Note that because of the vertical extension of the domain, we can only probe k_z in multiples of 10π. The maximum growth rates obtained from PLUTO are shown in Fig. 7 together with the predicted maximum growth rates from the global eigenvalue analysis. Fig. 7 can also be compared with the left-hand panels of Fig. 2. We recover the suppression of the MRI growth rate at $v_{A\phi} = 0.3$, as predicted by PP05. Above $v_{A\phi} = 0.3$, we also see the appearance of the new instabilities, namely, SHMI (see e.g. the non-zero $\omega_{\rm I\,max}$ for $k_z = 31$, $62 < k_{\rm SI}$ for $v_{A\phi} = 0.4$) and SSMI (see e.g. the non-zero $\omega_{\rm I\,max}$ for $k_z = 125 > k_{\rm SI}$ for $v_{A\phi} = 0.4$, recalling from the eigenvalue analysis that $k_{\rm SI} \approx 93$ for this field strength). The lowest dispersion (σ) between the numerical and theoretical growth rates is obtained for $v_{A\phi} = 0.1$, with an

average dispersion on the four largest modes being $\sigma = 0.01$ (i.e. less than 2 per cent in relative error), while the highest error is obtained for $v_{A\phi} = 0.4$, with $\sigma = 0.07$. Larger discrepancies are observed when small-scale modes grow much faster than large-scale ones, in which case our Fourier transform method gets contaminated by the fast-growing modes at small scales. This contamination becomes especially important when the magnetic field is highly suprathermal, i.e. $v_{A\phi} > 0.3$, since the small-scale SSMI modes can have larger growth rates compared to the large-scale SHMI modes.

7 SUMMARY AND CONCLUSIONS

Below we summarize the main findings of our analysis:

(i) We have performed a detailed, global eigenvalue analysis of the linearized, axisymmetric, MHD equations of a differentially rotating fluid in cylindrical geometry, in order to carry out a stability analysis of strongly magnetized accretion flows. We confirm that MRI growth rates tend to get highly suppressed in the presence of a sufficiently suprathermal toroidal magnetic field, when the geometric curvature effects as well as compressibility of the flow are taken into account. The current work hence validates one of the main claims of PP05, who performed a linear stability analysis of a similar accretion flow but under the local approximation. However, there are some differences between the outcomes of the global and local analyses, which we discuss below. Note that both the current work and PP05 neglect the effects of non-axisymmetry and spatial gradients in the background variables.

(ii) We have recovered in our global calculations that when a limiting toroidal Alfvén velocity is reached, the MRI growth rate starts to decline sharply. This limit is given by the square root of the product of the Keplerian velocity at the inner radius and the sound speed, in agreement with the PP05 prediction. However, unlike PP05, we do not observe a complete stabilization at low vertical wavenumbers at this limit, but instead recover a low growth rate tail extending all the way to $k_z = 0$. When a *second* limit in the toroidal Alfvén velocity is reached, which is a factor $\sqrt{2}$ higher than the previous one, the MRI growth rate drops to only a few per cent of the maximum value for standard MRI (which has zero or very weak background toroidal field), as predicted by PP05. However, we find that as long as MRI operates in the global analysis, it extends across the entire range of allowed vertical wavenumbers satisfying the classic Balbus–Hawley criterion of $k_z < k_{\rm MRI}$, where $(k_{\rm MRI} v_{Az})^2 \approx -\partial\Omega^2/\partial \ln r$. This is contrary to PP05, who predicted that the MRI stabilization gradually progresses from low to higher vertical wavenumbers as the background toroidal field strength increases.

(iii) We have observed, similar to PP05, the emergence of two new instabilities in the suprathermal regime beyond the second PP05 limit in our global calculations. However, the global properties of these instabilities are somewhat different from the local prediction. These two instabilities are, namely, the SSMI and the SHMI. We have established that SSMI is a slow-mode instability like MRI, while SHMI is a hybrid mode that results from a destabilized slow-Alfvén mode coupling and, hence, the nomenclature. In the PP05 case, SSMI and SHMI operate in well-separated vertical wavenumber regimes. For the same toroidal Alfvén velocity, SHMI appears in a *limited* wavenumber range $0 < k_z < k_{c1}$, while SSMI appears at $k_z > k_{c1}$. The global analysis exhibits two majors differences in this respect. First, SHMI in the global case extends all the way to $k_z = 0$, unlike in the PP05 case. Second, there is an overlap in the growth rate of the *most* unstable modes of SHMI and SSMI at a new critical wavenumber $k_{\rm SI}$ that emerges in the global analysis. Thus, the most unstable modes of SSMI arise before those of SHMI can stabilize completely in the $\omega_{\rm I} - k_z$ space. There is, however, a sharp discontinuity in the phase velocity of the most unstable modes of these two instabilities at $k_{\rm SI}$ in the $\omega_{\rm R} - k_z$ space. This, together with the fact that SHMI and SSMI have different physical origins, establish them to be two distinct modes in the global case. We have further verified that SSMI stabilizes at a small but finite length-scale in accordance with the PP05 stability criteria. Thus, in the global analysis, the most unstable modes of SHMI occupy the range $0 \leq k_z \leq k_{c1}$, whereas those of SSMI occupy the whole range $k_{\rm SI} \leq k_z \leq k_{c2}$, where $k_{\rm SI}$ marks *both* the maximum allowed wavenumber for the *most* unstable modes of SHMI as well as the minimum onset wavenumber for those of SSMI. The growth rates and the wavenumber occupancies of both instabilities were seen to increase with an increase in the background toroidal field strength. The coexistence of SHMI and SSMI, for the same suprathermal toroidal field, leads to the interesting question of whether the SHMI could feed energy into the SSMI modes and vice versa in the non-linear regime.

(iv) On the analytical front, we have self-consistently derived a generic, local dispersion relation, by using a physically motivated WKB formalism. A local dispersion relation is useful in not only providing analytical insight into the problem but also for comparing with the global calculations. Our dispersion relation includes the effects of compressibility and magnetic curvature, as well as non-axisymmetry and background radial gradients. We have further considered the effect of magnetic tension in the background equilibrium flow, in order to self-consistently take into account the deviation from Keplerian flow at strong magnetic field strengths.

(v) We have computed the normalized radial eigenfunctions of the most unstable modes in the global analysis, which are not obtainable from a local calculation. Interestingly, we have found that in the presence of a suprathermal field, the eigenfunctions of the most unstable modes exhibit different radial localizations. This is in contrast with standard MRI, where the most unstable modes are *all* localized close to the inner radial boundary, in keeping with MRI as a purely shear-driven instability. There also seems to exist a positive correlation between the number of radial nodes and the radial extent of the eigenfunctions. All this might be an indication of the possible driving mechanisms for the different suprathermal instabilities. The modes that are localized close to the inner radial boundary are likely to be shear driven, whereas the modes that are more radially extended are likely to be driven by radial buoyancy, which is generated from the magnetic tension force of the suprathermal toroidal field.

(vi) We have studied the eigenspectra of the large family of global modes for different suprathermal fields. They display complex structures in the $\omega_R - \omega_I$ plane, which establishes that all the instabilities, MRI, SHMI and SSMI, are in general overstable in the presence of a suprathermal toroidal field. This is contrary to the standard weak-field MRI, which is purely unstable.

(vii) We have also verified the main results of our linear eigenvalue analysis by performing a small set of numerical simulations using PLUTO. The suppression of the MRI growth rates is clearly recovered at the critical suprathermal toroidal field strength mentioned above. For toroidal field strengths beyond this critical value, the new instabilities SSMI and SHMI are also recovered. However, for very high suprathermal fields, there is greater discrepancy between the growth rates from the simulations and the eigenvalue analysis. This might be a result of the increased numerical diffusion at these field strengths, as well as contamination from fast growing modes at small scales.

Thus, all the above findings underline the need for a global treatment to accurately capture the curvature effects due to a suprathermal toroidal field. Note that in this work, we have assumed the presence of an already suprathermal field, which is motivated by the results of shearing box simulations (see e.g. Bai & Stone 2013; Salvesen et al. 2016a,b). The development of a such a field shows that MRI can overcome buoyancy effects in shearing box simulations. However, shearing boxes cannot take magnetic curvature effects into consideration, which is where the relevance of the current work sets in. The fact that we observe a bottleneck in the MRI growth leads to the important question of whether it ultimately limits the creation of highly suprathermal toroidal fields in real accretion discs. Our analysis can serve as a benchmark for global, vertically stratified simulations, which are necessary to truly understand the physics of magnetically dominated systems. While there have been a few such simulations of strongly magnetized accretion discs (Machida, Hayashi & Matsumoto 2000; Gaburov, Johansen & Levin 2012; Sądowski 2016; Fragile & Sądowski 2017), more work needs to be done to specifically address and unravel the nature of instabilities in the strongly magnetized regime.

ACKNOWLEDGEMENTS

This work was supported in part by NASA Astrophysics Theory Program grant NNX14AB37G and NSF grant AST-1411879. UD is immensely grateful to Ben Brown for allocating time on the LCD machines, where all the calculations using Dedalus were performed, as well as for useful discussions. UD specially thanks Evan Anders and Jeff Oishi for their help in navigating through Dedalus and Vladimir Zhdankin for general discussions. The authors thank the anonymous referee for their constructive comments.

REFERENCES

Bai X.-N., Stone J. M., 2013, ApJ, 767, 30
Balbus S. A., 1995, ApJ, 453, 380
Balbus S. A., Hawley J. F., 1991, ApJ, 376, 214
Balbus S. A., Hawley J. F., 1992, ApJ, 392, 662
Balbus S. A., Hawley J. F., 1998, Rev. Mod. Phys., 70, 1
Begelman M. C., 1998, ApJ, 493, 291
Begelman M. C., Pringle J. E., 2007, MNRAS, 375, 1070
Begelman M. C., Armitage P. J., Reynolds C. S., 2015, ApJ, 809, 118
Béthune W., Lesur G., Ferreira J., 2016, A&A, 589, A87
Blaes O. M., Balbus S. A., 1994, ApJ, 421, 163
Blaes O., Socrates A., 2001, ApJ, 553, 987
Boyd J. P., 2001, Chebyshev and Fourier Spectral Methods. Dover Publications, Mineola, NY, p. 2001
Curry C., Pudritz R. E., 1995, ApJ, 453, 697
Curry C., Pudritz R. E., Sutherland P. G., 1994, ApJ, 434, 206
Fragile P. C., Sądowski A., 2017, MNRAS, 467, 1838
Fromang S., Latter H., Lesur G., Ogilvie G. I., 2013, A&A, 552, A71
Gaburov E., Johansen A., Levin Y., 2012, ApJ, 758, 103
Kersalé E., Hughes D. W., Ogilvie G. I., Tobias S. M., Weiss N. O., 2004, ApJ, 602, 892
Kim W.-T., Ostriker E. C., 2000, ApJ, 540, 372
Latter H. N., Fromang S., Faure J., 2015, MNRAS, 453, 3257
Lesur G., Ferreira J., Ogilvie G. I., 2013, A&A, 550, A61
Lightman A. P., Eardley D. M., 1974, ApJ, 187, L1
Machida M., Hayashi M. R., Matsumoto R., 2000, ApJ, 532, L67
Mignone A., Bodo G., Massaglia S., Matsakos T., Tesileanu O., Zanni C., Ferrari A., 2007, ApJS, 170, 228
Miller K. A., Stone J. M., 2000, ApJ, 534, 398
Miller J. M., Raymond J., Fabian A., Steeghs D., Homan J., Reynolds C., van der Klis M., Wijnands R., 2006, Nature, 441, 953
Miller J. M. et al., 2016, ApJ, 821, L9
Moll R., 2012, A&A, 548, A76
Oda H., Machida M., Nakamura K. E., Matsumoto R., 2009, ApJ, 697, 16
Pariev V. I., Blackman E. G., Boldyrev S. A., 2003, A&A, 407, 403
Pessah M. E., Psaltis D., 2005, ApJ, 628, 879 (PP05)
Riols A., Ogilvie G. I., Latter H., Ross J. P., 2016, MNRAS, 463, 3096
Salvesen G., Armitage P. J., Simon J. B., Begelman M. C., 2016a, MNRAS, 460, 3488
Salvesen G., Simon J. B., Armitage P. J., Begelman M. C., 2016b, MNRAS, 457, 857
Shakura N. I., Sunyaev R. A., 1973, A&A, 24, 337

Shakura N. I., Sunyaev R. A., 1976, MNRAS, 175, 613
Sądowski A., 2016, MNRAS, 459, 4397
Terquem C., Papaloizou J. C. B., 1996, MNRAS, 279, 767 (TP96)

APPENDIX A: CORRECTION FOR NON-ADIABATIC BACKGROUND

In the analysis presented in Section 3.2, we assumed the background to be adiabatic and, hence, ignored the non-adiabacity $\boldsymbol{S}$ given by equation (17). Here, we relax this assumption.

If we retrace one step, then the second term on the right-hand side of equation (25) is actually $(\rho_1/\rho_0)\rho_0 r(\Omega^2 - \Omega_{\rm K}^2)$, where

$$\frac{\rho_1}{\rho_0} = \frac{P_1}{\gamma P_0} - \frac{i v_{1{\rm r}}}{m\Omega - \omega} S_{\rm r} \tag{A1}$$

and

$$S_{\rm r} = \partial_{\rm r}\left(\ln \frac{P_0^{1/\gamma}}{\rho_0}\right). \tag{A2}$$

We included the first, but not the second term of equation (A1) in equation (25) and the following steps. Making the appropriate corrections in the following steps, the dispersion relation given by equation (40) is modified in the presence of a non-adiabatic background to

$$\left[(x\mu^2 - n^2)\left(1 + \frac{l^2}{k_{\rm z}^2}\right) + xyrS_{\rm r} + (2+y)(1+\hat{B}_\phi)\right]\left[n^2 - (1+x)\mu^2\right] + 2(2-q)x(1+x)\mu^2\tilde{\Omega}^2 + 4\mu x n\tilde{\Omega}(2+y) + 2n^2 qx\tilde{\Omega}^2 + x\mu^2(2+y)^2 = 0. \tag{A3}$$

APPENDIX B: LIMITING CASES OF THE LOCAL DISPERSION RELATION

Here, we show that the dispersion relation given by equation (A3) reduces to well-known dispersion relations under various limits, which further validates our analytical calculations.

(i) *Non-rotating, no-gravity limit* (Begelman 1998): We put $\tilde{\Omega} = \tilde{\Omega}_{\rm K} = 0$ and, hence, $y = 0$, which reduces equation (A3), on some rearrangement, to

$$\frac{1}{2}(x\mu^2 - n^2)\left(1 + \frac{l^2}{k_{\rm z}^2}\right) + \frac{n^2 - (1-x)\mu^2}{n^2 - (1+x)\mu^2} + \hat{B}_\phi = 0. \tag{B1}$$

This is identical to the dispersion relation given by equation (3.32) of Begelman (1998), which describes current-driven instabilities of a static MHD pinch.

(ii) *Axisymmetric, incompressible, weak*-$\mathrm{B}_{0\phi}$*, no-curvature limit* (Balbus & Hawley 1998): We put $m = 0$ and, hence, $n = \eta$ and $\mu = \tilde{\omega}$, in order to get the axisymmetric dispersion relation from equation (A3). In addition, we put $\hat{B}_\phi = 0$ and take $x \to \infty$, $\eta \propto \sqrt{x}$ and everything else finite, which reduces equation (A3) after some rearrangement to

$$\left(\tilde{\omega}^2 - \frac{\eta^2}{x}\right)\left(1 + \frac{l^2}{k_{\rm z}^2}\right) + yrS_{\rm r} - \frac{2\tilde{\Omega}^2\left[(2-q)\tilde{\omega}^2 + q\frac{\eta^2}{x}\right]}{\left(\tilde{\omega}^2 - \frac{\eta^2}{x}\right)} = 0. \tag{B2}$$

Now, in order to compare equation (B2) with Balbus & Hawley (1998), we have to make it dimensionful. Recalling the definitions from Table 1 and equation (8), and by multiplying equation (B2) throughout by $c_{\rm s}^4/r^4$, we obtain after some rearrangement

$$\left(\omega^2 - k_{\rm z}^2 v_{\rm Az}^2\right)^2\left(1 + \frac{l^2}{k_{\rm z}^2}\right) + \left[S_{\rm r}\frac{1}{\rho_0}\partial_{\rm r}P_0 + \frac{1}{r^3}\partial_{\rm r}(r^4\Omega^2)\right](\omega^2 - k_{\rm z}^2 v_{\rm Az}^2) - 4\Omega^2(k_{\rm z}^2 v_{\rm Az}^2) = 0. \tag{B3}$$

We can hence show that equation (B3) is equivalent to equation (125) of Balbus & Hawley (1998), after correcting the typo in the latter [i.e. $\mathcal{D}(R^4\Omega^4) \to \mathcal{D}(R^4\Omega^2)$] and identifying the following:

$$(\omega^2 - k_{\rm z}^2 v_{\rm Az}^2) \equiv \varpi;\ \ k_{\rm z}^2 v_{\rm Az}^2 \equiv (\boldsymbol{k}\cdot\boldsymbol{u}_{\rm A})^2;\ \ \left(1 + \frac{l^2}{k_{\rm z}^2}\right) \equiv \frac{k^2}{k_{\rm z}^2};\ \ r \equiv R;$$
$$\partial_{\rm r} \equiv \mathcal{D};\ \ P_0 \equiv P;\ \ \rho_0 \equiv \rho;\ \ S_{\rm r} \equiv -\frac{1}{\gamma}\mathcal{D}\left(\frac{\ln P}{\rho^\gamma}\right)\tilde{}. \tag{B4}$$

(iii) *No poloidal field limit* (TP96): We first put $\eta = 0$ and, hence, $n = m$ in equation (A3), which on expanding and dividing throughout by $x(x+1)k^2/k_{\rm z}^2$, where $k^2 = l^2 + k_{\rm z}^2$, yields

$$\mu^4 + \left[-\frac{m^2}{x}\frac{(1+2x)}{(1+x)} + 2q\frac{k_z^2}{k^2}\tilde{\Omega}^2 - 4\frac{k_z^2}{k^2}\tilde{\Omega}^2 + \frac{k_z^2}{k^2} yr S_r - \frac{k_z^2}{k^2}\frac{(2+y)^2}{(1+x)} + \frac{k_z^2}{k^2}\frac{(2+y)(1+\hat{B}_\phi)}{x} \right]\mu^2 - 4\frac{k_z^2}{k^2}\frac{(2+y)}{(1+x)} m\tilde{\Omega}\mu$$
$$- \frac{m^2}{(1+x)}\frac{k_z^2}{k^2}\left[-\frac{k^2}{k_z^2}\frac{m^2}{x} + yr S_r + 2q\tilde{\Omega}^2 + \frac{(2+y)(1+\hat{B}_\phi)}{x} \right] = 0 \tag{B5}$$

or

$$\mu^4 + \tilde{\alpha}\mu^2 - \tilde{\beta}\mu + \tilde{\delta} = 0. \tag{B6}$$

The corresponding dispersion relation (dimensionful) from TP96 is given by their equation (33) as

$$\bar{\sigma}^4 + \alpha_{\rm TP}\bar{\sigma}^2 + \beta_{\rm TP}\bar{\sigma} + \delta_{\rm TP} = 0, \tag{B7}$$

where $\bar{\sigma} = \sigma_{\rm TP} + m\Omega$ such that the time dependence of the perturbations are of the form $\exp(i\sigma_{\rm TP}t)$; $\alpha_{\rm TP}$, $\beta_{\rm TP}$ and $\delta_{\rm TP}$ are given by equations (29), (30) and (34) of TP96 respectively. We next show that these two equations (B6) and (B7) are in fact identical when we set the vertical background gradients in equation (B7) to be zero.

In order to compare the two dispersion relations, we have to first non-dimensionalize equation (B7) according to our prescription such that

$$\mu \equiv -\bar{\sigma}\frac{r}{c_s};\ \ \tilde{\alpha} \equiv \alpha_{\rm TP}\frac{r^2}{c_s^2};\ \ \tilde{\beta} \equiv \beta_{\rm TP}\frac{r^3}{c_s^3};\ \ \tilde{\delta} \equiv \delta_{\rm TP}\frac{r^4}{c_s^4}. \tag{B8}$$

First, we consider the coefficient of the quadratic terms in the two dispersion relations. Equation (29) of TP96 reduces, in terms of our notation (see Table 1) to

$$\alpha_{\rm TP}\frac{r^2}{c_s^2} = -\frac{m^2}{x}\frac{(1+2x)}{(1+x)} + 2q\frac{k_z^2}{k^2}\tilde{\Omega}^2 - 4\frac{k_z^2}{k^2}\tilde{\Omega}^2 + \left(\frac{x}{1+x}\right)\frac{k_z^2}{k^2}\left(y - \frac{2}{x}\right)^2 - \frac{k_z^2}{k^2} y\left(\frac{r\partial_r\rho_0}{\rho_0}\right) + \frac{2}{x}\frac{k_z^2}{k^2}(\hat{B}_\phi - 1). \tag{B9}$$

We see that the first three terms in the above equation match exactly with the first three terms in the coefficient of μ^2 (i.e. $\tilde{\alpha}$) in equation (B5). Cancelling the common factor of k_z^2/k^2, we therefore need to show that the remaining terms between equations (B5) and (B9) also agree, namely

$$yr S_r - \frac{(2+y)^2}{(1+x)} + \frac{(2+y)(1+\hat{B}_\phi)}{x} = \left(\frac{x}{1+x}\right)\left(y - \frac{2}{x}\right)^2 - y\left(\frac{r\partial_r\rho_0}{\rho_0}\right) + \frac{2}{x}(\hat{B}_\phi - 1). \tag{B10}$$

Using equations (8) and (A2), we can write

$$-\frac{r\partial_r\rho_0}{\rho_0} = rS_r - r\frac{\partial_r P_0}{\gamma P_0} = rS_r - y + \frac{1+\hat{B}_\phi}{x}. \tag{B11}$$

The above, when replaced on the right-hand side of equation (B10), makes it identical to the left-hand side. This establishes that the coefficient of μ^2 in our dispersion relation (equation B5) agrees with that of TP96.

Similarly, we can show the coefficient of the linear terms as well as the constant terms are identical between the two dispersion relations. Thus, our dispersion relation given by equation (A3) is equivalent to that of TP96, when $n = m$ and the background state depends only on r.

This paper has been typeset from a TEX/LATEX file prepared by the author.